

# Antenna Design Techniques for 5G Mobile Communications

Lead Guest Editor: Khalil H. Sayidmarie

Guest Editors: Raed A. Abd-Alhameed, Peter Excell, Chan H. See, Issa Elfergani, and Jonathan Rodriguez





---

# **Antenna Design Techniques for 5G Mobile Communications**

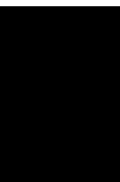
Wireless Communications and Mobile Computing

---

## **Antenna Design Techniques for 5G Mobile Communications**

Lead Guest Editor: Khalil H. Sayidmarie

Guest Editors: Raed A. Abd-Alhameed, Peter  
Excell, Chan H. See, Issa Elfergani, and Jonathan  
Rodriguez




---



Copyright © 2020 Hindawi Limited. All rights reserved.

This is a special issue published in “Wireless Communications and Mobile Computing.” All articles are open access articles distributed under the Creative Commons Attribution License, which permits unrestricted use, distribution, and reproduction in any medium, provided the original work is properly cited.

# Chief Editor

Zhipeng Cai , USA

## Associate Editors

Ke Guan , China  
Jaime Lloret , Spain  
Maode Ma , Singapore

## Academic Editors

Muhammad Inam Abbasi, Malaysia  
Ghufran Ahmed , Pakistan  
Hamza Mohammed Ridha Al-Khafaji ,  
Iraq  
Abdullah Alamoodi , Malaysia  
Marica Amadeo, Italy  
Sandhya Aneja, USA  
Mohd Dilshad Ansari, India  
Eva Antonino-Daviu , Spain  
Mehmet Emin Aydin, United Kingdom  
Parameshchhari B. D. , India  
Kalapaveen Bagadi , India  
Ashish Bagwari , India  
Dr. Abdul Basit , Pakistan  
Alessandro Bazzi , Italy  
Zdenek Becvar , Czech Republic  
Nabil Benamar , Morocco  
Olivier Berder, France  
Petros S. Bithas, Greece  
Dario Bruneo , Italy  
Jun Cai, Canada  
Xuesong Cai, Denmark  
Gerardo Canfora , Italy  
Rolando Carrasco, United Kingdom  
Vicente Casares-Giner , Spain  
Brijesh Chaurasia, India  
Lin Chen , France  
Xianfu Chen , Finland  
Hui Cheng , United Kingdom  
Hsin-Hung Cho, Taiwan  
Ernestina Cianca , Italy  
Marta Cimitile , Italy  
Riccardo Colella , Italy  
Mario Collotta , Italy  
Massimo Condoluci , Sweden  
Antonino Crivello , Italy  
Antonio De Domenico , France  
Floriano De Rango , Italy

Antonio De la Oliva , Spain  
Margot Deruyck, Belgium  
Liang Dong , USA  
Praveen Kumar Donta, Austria  
Zhuojun Duan, USA  
Mohammed El-Hajjar , United Kingdom  
Oscar Esparza , Spain  
Maria Fazio , Italy  
Mauro Femminella , Italy  
Manuel Fernandez-Veiga , Spain  
Gianluigi Ferrari , Italy  
Luca Foschini , Italy  
Alexandros G. Fragkiadakis , Greece  
Ivan Ganchev , Bulgaria  
Óscar García, Spain  
Manuel García Sánchez , Spain  
L. J. García Villalba , Spain  
Miguel Garcia-Pineda , Spain  
Piedad Garrido , Spain  
Michele Girolami, Italy  
Mariusz Glabowski , Poland  
Carles Gomez , Spain  
Antonio Guerrieri , Italy  
Barbara Guidi , Italy  
Rami Hamdi, Qatar  
Tao Han, USA  
Sherief Hashima , Egypt  
Mahmoud Hassaballah , Egypt  
Yejun He , China  
Yixin He, China  
Andrej Hrovat , Slovenia  
Chunqiang Hu , China  
Xuexian Hu , China  
Zhenghua Huang , China  
Xiaohong Jiang , Japan  
Vicente Julian , Spain  
Rajesh Kaluri , India  
Dimitrios Katsaros, Greece  
Muhammad Asghar Khan, Pakistan  
Rahim Khan , Pakistan  
Ahmed Khattab, Egypt  
Hasan Ali Khattak, Pakistan  
Mario Kolberg , United Kingdom  
Meet Kumari, India  
Wen-Cheng Lai , Taiwan




Jose M. Lanza-Gutierrez, Spain  
Pavlos I. Lazaridis , United Kingdom  
Kim-Hung Le , Vietnam  
Tuan Anh Le , United Kingdom  
Xianfu Lei, China  
Jianfeng Li , China  
Xiangxue Li , China  
Yaguang Lin , China  
Zhi Lin , China  
Liu Liu , China  
Mingqian Liu , China  
Zhi Liu, Japan  
Miguel López-Benítez , United Kingdom  
Chuanwen Luo , China  
Lu Lv, China  
Basem M. ElHalawany , Egypt  
Imadeldin Mahgoub , USA  
Rajesh Manoharan , India  
Davide Mattera , Italy  
Michael McGuire , Canada  
Weizhi Meng , Denmark  
Klaus Moessner , United Kingdom  
Simone Morosi , Italy  
Amrit Mukherjee, Czech Republic  
Shahid Mumtaz , Portugal  
Giovanni Nardini , Italy  
Tuan M. Nguyen , Vietnam  
Petros Nicolaitidis , Greece  
Rajendran Parthiban , Malaysia  
Giovanni Pau , Italy  
Matteo Petracca , Italy  
Marco Picone , Italy  
Daniele Pinchera , Italy  
Giuseppe Piro , Italy  
Javier Prieto , Spain  
Umair Rafique, Finland  
Maheswar Rajagopal , India  
Sujan Rajbhandari , United Kingdom  
Rajib Rana, Australia  
Luca Reggiani , Italy  
Daniel G. Reina , Spain  
Bo Rong , Canada  
Mangal Sain , Republic of Korea  
Praneet Saurabh , India

Hans Schotten, Germany  
Patrick Seeling , USA  
Muhammad Shafiq , China  
Zaffar Ahmed Shaikh , Pakistan  
Vishal Sharma , United Kingdom  
Kaize Shi , Australia  
Chakchai So-In, Thailand  
Enrique Stevens-Navarro , Mexico  
Sangeetha Subbaraj , India  
Tien-Wen Sung, Taiwan  
Suhua Tang , Japan  
Pan Tang , China  
Pierre-Martin Tardif , Canada  
Sreenath Reddy Thummaluru, India  
Tran Trung Duy , Vietnam  
Fan-Hsun Tseng, Taiwan  
S Velliangiri , India  
Quoc-Tuan Vien , United Kingdom  
Enrico M. Vitucci , Italy  
Shaohua Wan , China  
Dawei Wang, China  
Huaqun Wang , China  
Pengfei Wang , China  
Dapeng Wu , China  
Huaming Wu , China  
Ding Xu , China  
YAN YAO , China  
Jie Yang, USA  
Long Yang , China  
Qiang Ye , Canada  
Changyan Yi , China  
Ya-Ju Yu , Taiwan  
Marat V. Yuldashev , Finland  
Sherali Zeadally, USA  
Hong-Hai Zhang, USA  
Jiliang Zhang, China  
Lei Zhang, Spain  
Wence Zhang , China  
Yushu Zhang, China  
Kechen Zheng, China  
Fuhui Zhou , USA  
Meiling Zhu, United Kingdom  
Zhengyu Zhu , China

# Contents




---

**Three-Dimensional Coprime Array for Massive MIMO: Array Configuration Design and 2D DOA Estimation**

Pan Gong , Tanveer Ahmed , and Jianfeng Li 

Research Article (14 pages), Article ID 2686257, Volume 2020 (2020)

**Partial ML Detection for Frequency-Asynchronous Distributed Alamouti-Coded (FADAC) OFDM**

Bong-seok Kim , Dongjun Na , and Kwonhue Choi 

Research Article (10 pages), Article ID 4319802, Volume 2019 (2019)

## Research Article

# Three-Dimensional Coprime Array for Massive MIMO: Array Configuration Design and 2D DOA Estimation

Pan Gong , Tanveer Ahmed , and Jianfeng Li 

College of Electronic and Information Engineering, Nanjing University of Aeronautics and Astronautics, Nanjing 211106, China

Correspondence should be addressed to Pan Gong; [gongpan@nuaa.edu.cn](mailto:gongpan@nuaa.edu.cn)

Received 25 July 2019; Revised 14 October 2019; Accepted 28 December 2019; Published 13 January 2020

Guest Editor: Raed A. Abd-Alhameed

Copyright © 2020 Pan Gong et al. This is an open access article distributed under the Creative Commons Attribution License, which permits unrestricted use, distribution, and reproduction in any medium, provided the original work is properly cited.

In massive multiple-input multiple-output (MIMO) systems, it is critical to obtain the accurate direction of arrival (DOA) estimation. Conventional three-dimensional array mainly focuses on the uniform array. Due to the dense arrangement of the sensors, the array aperture is limited and severe mutual coupling effects arise. In this paper, a coprime cubic array (CCA) configuration design is presented, which is composed of two uniform cubic subarrays and can extend the interelement spacing with a selection of three pairs of coprime integers. Compared with uniform cubic array (UCA), CCA achieves the larger array aperture and less MC effects. And the analytical expression of Cramer–Rao Bound (CRB) for CCA is derived which verifies that the proposed CCA geometry outperforms the conventional UCA in two-dimensional (2D) DOA estimation performance in massive MIMO systems. Meanwhile, we propose a computationally efficient 2D DOA estimation algorithm with high accuracy for CCA. Specifically, we utilize array mapping to extract two uniform arrays from the nonuniform array by exploiting the relation derived from the signal subspace and the two directional matrices. Then, we operate a reduced dimension process on the uniform arrays and convert the 2D spectrum peak searching (SPS) problem into one-dimensional (1D) one, which significantly reduces the computational complexity. In addition, we employ the polynomial root finding technique with a lower complexity instead of 1D SPS to further relieve the computational complexity. Simultaneously, with coprime property, the phase ambiguity problem is solved, which results from the large interelement spacing. Numerical simulation results demonstrate that the proposed algorithm is very computationally efficient without degradation of DOA estimation performance.

## 1. Introduction

Nowadays, massive multiple-input multiple-output (MIMO), known as large-scale MIMO, is considered as one of the promising technologies in the development of future wireless communication systems. Massive MIMO attracts considerable attention due to the high throughput, enhanced link reliability, and improved spectral efficiency [1, 2]. Also, massive MIMO can effectively reduce the latency and robustness to interference [3, 4], which are important factors in wireless communication systems.

Direction of arrival (DOA) estimation plays an important role in massive MIMO, since precise DOA estimation is vital for the base station (BS) to conduct downlink precoding or beamforming [5]. DOA estimation is also widely utilized in engineering applications, like radar, sonar, wireless

communication, and navigation [6–9]. Many classic DOA estimation algorithms [10–13] and plenty of derived algorithms [14–16] have been proposed to solve the DOA estimation problem. Most of these existing algorithms mainly utilize the conventional uniform array configurations [17, 18] with the interelement spacing no larger than typical half-wavelength to tackle the problem of phase ambiguity [19]. However, in the massive MIMO systems, with a large number of antennas, severe mutual coupling (MC) effects arise, which significantly affect the DOA estimation accuracy.

In recent years, a new configuration called coprime array [20] has been a hot research direction and attracts much attention since it can significantly enhance the degree of freedom (DOF) [21], improve the resolution [22], and relieve MC effects [23]. This motivates many studies of DOA



estimation using coprime array over the decade. In [24], a total angular search based algorithm by employing the multiple signals classification (MUSIC) algorithm was proposed. By exploiting the coprime property, the phase ambiguity problem is tackled. In [25], an ambiguity-free DOA estimation algorithm was proposed, which exploits the total information including self-information and mutual information to eliminate the ambiguity problem with high accuracy of DOA estimates. However, due to the total angular search, this algorithm results in large computational complexity. To deal with this obstacle, a partial spectral search (PSS) algorithm was introduced which only performs spectrum searching in a restricted sector and hence lowers the computational cost but has no effect on DOA estimation performance [26]. In the case of multiple sources, this algorithm will cause the target matching error when eliminating the phase ambiguity. To tackle the problem, an improved DOA estimation algorithm based on root-MUSIC was proposed in [27] for coprime linear array (CLA), which employs the relation between steering matrices and signal subspaces of two subarrays to achieve DOA estimation.

The algorithms mentioned above [24–27] were presented for one-dimensional (1D) DOA estimation, whereas, practically, two-dimensional (2D) DOA estimation possesses more importance, and various studies have been introduced [28–30]. In [28], the PSS algorithm for coprime planar array (CPA) was presented, which can reduce the computational complexity. A reduced dimension notion to achieve 2D DOA estimation was proposed in [29]. A generalized CPA geometry with more flexible array layouts was constructed for 2D DOA estimation [30], which can attain more DOFs compared with CPA configuration. However, spectrum peak searching (SPS) is involved in these mentioned works [28–30] and hence causes expensive computational cost.

In this paper, on the basis of the 1D CLA and 2D CPA, we construct a three-dimensional (3D) array geometry called coprime cubic array (CCA). In the context of massive MIMO systems [31, 32], MC effects become important which have a vital influence on DOA estimation accuracy. The geometry of CCA possesses the extended array aperture and can effectively reduce MC effects. Especially, in the cases with small elevations, the CCA obtains superior DOA estimation performance. Simultaneously, the Cramer–Rao Bound (CRB) is derived which demonstrates that the proposed CCA geometry outperforms the conventional uniform cubic array (UCA) configuration [33–35]. In addition, we propose an array mapping and reduced dimension based on computationally efficient MUSIC (AMRD-MUSIC) algorithm to estimate 2D DOAs. Different from the conventional multiple-dimensional MUSIC (MD-MUSIC) algorithm, where 2D SPS involves a tremendous computation burden, in the proposed algorithm, we utilize array mapping to extract two uniform arrays from the nonuniform array by exploiting the relation derived from the signal subspace and the two directional matrices. Then, we operate a reduced dimension process on the uniform arrays and convert the 2D spectrum peak searching (SPS) problem into 1D one, which significantly reduces the computational

complexity. In addition, we employ the polynomial root finding technique with a lower complexity instead of 1D SPS to further reduce the computational complexity. Meanwhile, according to the coprime property, the phase ambiguity problem is solved which results from large interelement spacing and the proposed algorithm obtains paired angles automatically. Numerical simulation results demonstrate that the proposed AMRD-MUSIC algorithm can significantly reduce the computational complexity cost with no degradation of DOA estimation performance.

Specifically, we summarize the main contributions of this paper.

- (1) In massive MIMO systems, conventional 3D array mainly focuses on the uniform array, which limits the array aperture and suffers from severe MC effects due to the dense location of sensors. We construct a CCA configuration which can achieve the larger array aperture and less MC effects compared with UCA. In addition, the analytical expression of CRB with CCA is derived and simulations demonstrate that the proposed CCA performs better DOA estimation performance than the conventional UCA configuration.
- (2) We propose an AMRD-MUSIC algorithm for 2D DOA estimation that can achieve almost the same DOA estimation performance as classic MD-MUSIC algorithm but with lower computational complexity. Through array mapping, we extract two uniform arrays from the nonuniform array and operate a reduced dimension on these two arrays to reduce 2D SPS into 1D one, which can effectively lower the computational complexity. To further reduce complexity, we utilize the polynomial root finding technique with a lower complexity instead of SPS. Therefore, computational complexity obtains a significant decrease.
- (3) The proposed algorithm can achieve the full DOFs and obtain DOA estimates with pairing automatically.

Section 2 introduces the array configuration and signal model. In Section 3 and Section 4, we present the proposed algorithm and analyse the performance of the proposed algorithm, respectively. Sections 5 and 6 provide numerical simulations and conclusions, respectively.

*Notations* 1. We use  $(\cdot)^T$  as the transpose, and  $(\cdot)^H$  is utilized as the conjugate transpose.  $\odot$  signifies *Khatri–Rao* product and  $\otimes$  denotes *Kronecker* product.  $E(\cdot)$  is expectation.  $D_m(\cdot)$  is a diagonal matrix that is formed of the  $m$ -th row of the matrix.  $\angle(\cdot)$  is a phase operator.

## 2. Array Configurations and Signal Model

*2.1. Uniform Cubic Array.* UCA geometry is designed with  $M \times N \times J$  sensors, where  $M$  denotes the number of sensors in the  $x$ -axis,  $N$  and  $J$  denote the number of sensors in the  $y$ -axis and  $z$ -axis, respectively. The interelement spacing of UCA is  $d_x = d_y = d_z = \lambda/2$ , which denotes the interelement

spacing of  $x$ -axis,  $y$ -axis, and  $z$ -axis, respectively.  $\lambda$  is wavelength. Figure 1(a) shows an example of UCA with  $M = N = J = 3$ .

**2.2. Coprime Cubic Array.** For UCA configuration, the array aperture is limited by the interelement spacing no larger than conventional half-wavelength. Simultaneously, MC effects exist due to the dense location of sensors. Based on CLA and CPA, we propose a CCA configuration, which can effectively increase the array aperture and decrease the MC effects.

**Definition 1** (coprime cubic array (CCA)). The CCA consists of two subarrays. The first subarray is composed of  $M_1 \times N_1 \times J_1$  sensors with the interelement spacing of  $d_{x1} = M_2\lambda/2$  in  $x$ -axis direction,  $d_{y1} = N_2\lambda/2$  in  $y$ -axis direction, and  $d_{z1} = J_2\lambda/2$  in  $z$ -axis direction. For the second subarray, it contains  $M_2 \times N_2 \times J_2$  elements and  $d_{x2} = M_1\lambda/2$ ,  $d_{y2} = N_1\lambda/2$ ,  $d_{z2} = J_1\lambda/2$ , where  $M_1, M_2, N_1, N_2$  and  $J_1, J_2$  are coprime integer pairs and stand for the number of sensors in  $x$ -axis,  $y$ -axis, and  $z$ -axis, respectively. Therefore, there are  $T_{CCA} = M_1N_1J_1 + M_2N_2J_2 - 1$  sensors in total. Figure 1(b) is an example of CCA geometry with  $M_1 = 3, N_1 = 2, J_1 = 3$  and  $M_2 = 2, N_2 = 3, J_2 = 2$ .

In the following part, we compare the array performance in array aperture and MC effects of UCA and CCA, respectively.

**2.3. Array Aperture Comparison.** In this subsection, we compare the array aperture of UCA and CCA in the same cases. For a fair comparison, we assume that the number of sensors in UCA and CCA is basically the same. According to [36], we can compute the array apertures of these arrays, which are denoted as  $\Gamma_{UCA}$  and  $\Gamma_{CCA}$ :

$$\Gamma_{UCA} = (M-1)(N-1)(J-1) \times \frac{\lambda^3}{8},$$

$$\Gamma_{CCA} = \max\left( (M_1-1)M_2(N_1-1)N_2(J_1-1)J_2 \frac{\lambda^3}{8}, \right. \\ \left. (M_2-1)M_1(N_2-1)N_1(J_2-1)J_1 \frac{\lambda^3}{8} \right). \quad (1)$$

For example, we set the UCA with  $M = 4, N = 4, J = 6$ , so the total number of sensors in UCA is  $T_{UCA} = M \times N \times J = 4 \times 4 \times 6 = 96$ . One subarray of CCA is of  $M_1 = 5, N_1 = 2, J_1 = 3$  and the other subarray is of  $M_2 = 4, N_2 = 3, J_2 = 5$ . The number of sensors in CCA is  $T_{CCA} = M_1 \times N_1 \times J_1 + M_2 \times N_2 \times J_2 - 1 = 89$  in total. We can note that the CCA has fewer number of sensors than UCA. As a result, for the two given arrays, the array aperture can be obtained as  $\Gamma_{UCA} = 5.625\lambda^3, \Gamma_{CCA} = 90\lambda^3$ . So we have

$$\Gamma_{UCA} < \Gamma_{CCA}. \quad (2)$$

It can be seen that the proposed CCA configuration can effectively enlarge the array aperture with fewer sensors.

**2.4. Mutual Coupling Effects Comparison.** Array signal models usually neglect the MC between the sensors. In practical application, the MC effects between the closely located sensors should be considered. Without loss of generality, we employ a coupling matrix  $\mathbf{C} \in \mathbb{C}^{T \times T}$ , where  $T$  denotes the total number of sensors in the array. In general, the expression of  $\mathbf{C}$  is very complicated. According to [37], for given UCA and CCA configurations,  $\mathbf{C}$  can be denoted approximately by a B-banded Toeplitz matrix as follows:

$$\mathbf{C}_{i,j} = \begin{cases} c_{|d_i-d_j|}, & |d_i-d_j| \leq B, \\ 0, & |d_i-d_j| > B, \end{cases} \quad (3)$$

where the value of  $\mathbf{C}_{i,j}$  is inversely proportional to sensor distance and satisfies  $1 = c_0 > |c_1| > |c_2| > \dots > |c_B| > |c_{B+1}| = 0$ .  $B$  is a constant and  $d_i$  denotes the positions of sensors.

According to [37], the coupling leakage can be exploited to evaluate the total MC

$$L = \frac{\|\mathbf{C} - \text{diag}(\mathbf{C})\|_F}{\|\mathbf{C}\|_F}, \quad (4)$$

where  $\|\mathbf{C} - \text{diag}(\mathbf{C})\|_F$  is the amount of MC. It is indicated that the smaller  $L$  is, the less MC is.

We compare the coupling leakages of the given UCA of  $M = 4, N = 4, J = 6$  and CCA of  $M_1 = 5, N_1 = 2, J_1 = 3$  and  $M_2 = 4, N_2 = 3, J_2 = 5$ . The total number of sensors of UCA and CCA is  $T_{UCA} = M \times N \times J = 4 \times 4 \times 6 = 96$  and  $T_{CCA} = M_1 \times N_1 \times J_1 + M_2 \times N_2 \times J_2 - 1 = 89$ , respectively. Hence, we have  $\mathbf{C}_{UCA} \in \mathbb{C}^{96 \times 96}$  and  $\mathbf{C}_{CCA} \in \mathbb{C}^{89 \times 89}$ . So the coupling coefficients can be computed by the following:

$$c_d = \begin{cases} 1, & d = 0, \\ 0.3e^{j\pi/3} \cdot \frac{e^{-j(d-1)\pi/8}}{d}, & 1 \leq d \leq B, \\ 0, & d > B, \end{cases} \quad (5)$$

where  $B = 3$  and  $d$  denotes the distance between the random two sensors. Then, we compute the coupling leakages of UCA and CCA as  $L(T_{UCA}) = 0.7588$  and  $L(T_{CCA}) = 0.2829$ , respectively. It can see that the proposed CCA can effectively decrease the MC effects.

$$L_{CCA} < L_{UCA}. \quad (6)$$

Table 1 shows the comparison of array aperture and coupling leakage for UCA and CCA in the same conditions. From Table 1, we can see that the proposed CCA configuration has the least sensors but outperforms the UCA in array aperture and MC effects. In addition, the CCA achieves better DOA estimation performance that is shown in Section 5. Therefore, in the following part, we employ the CCA into consideration.

**2.5. Signal Model.** Assume that there are  $K$  far-field uncorrelated narrowband incident signals impinging on the CCA from  $\{(\theta_k, \phi_k) \mid \theta_k \in (0^\circ, 90^\circ), \phi_k \in (0^\circ, 180^\circ)\}$ ,

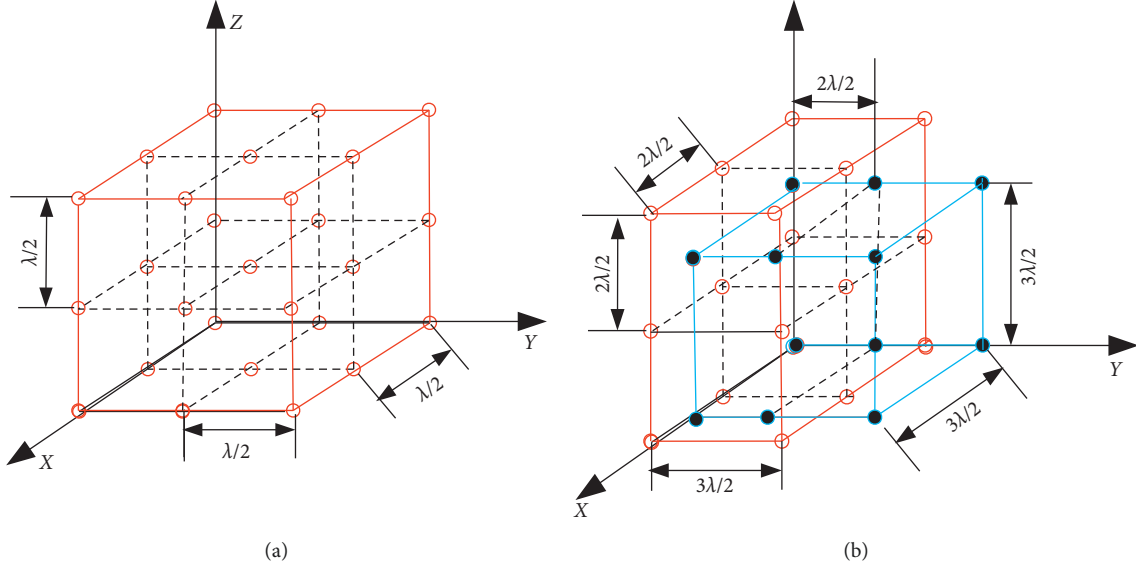


FIGURE 1: Array configurations. (a) The structure of UCA ( $M = N = J = 3$ ) and (b) the structure of CCA ( $M_1 = 3, N_1 = 2, J_1 = 3$  and  $M_2 = 2, N_2 = 3, J_2 = 2$ ).

TABLE 1: Performance of the array configurations.

Configuration	Total number of sensors	Array aperture	Coupling leakage
UCA	96	$5.625\lambda^3$	0.7588
CCA	89	$90\lambda^3$	0.2829

$k = 1, 2, \dots, K$ }, where  $\theta_k$  and  $\phi_k$  denote the DOA (the elevation angle and azimuth angle) of the  $k$ -th target [19]. And we define  $K < \min\{M_1 N_1 J_1, M_2 N_2 J_2\}$ ,  $u_k = \sin \theta_k \cos \phi_k \in (-1, 1)$ ,  $v_k = \sin \theta_k \sin \phi_k \in (0, 1)$ , and  $w_k = \cos \theta_k \in (0, 1)$ . In the following, we take the subarray that has  $M_i \times N_i \times J_i$  ( $i = 1, 2$ ) sensors to derive the proposed algorithm in the following part.

We denote the received signal as follows [28]:

$$\mathbf{x}_i(t) = \mathbf{A}_i \mathbf{s}(t) + \mathbf{n}_i(t), \quad i = 1, 2, \quad (7)$$

where  $\mathbf{s}(t) = [s_1(t), s_2(t), \dots, s_K(t)] \in \mathbb{C}^{K \times L}$  represents the signal matrix and  $L$  denotes the number of snapshots.  $\mathbf{n}_i \in \mathbb{C}^{M_i N_i J_i \times L}$  is the additive white Gaussian noise matrix, whose variance and mean are  $\sigma_n^2$  and zero, respectively.  $\mathbf{A}_i \in \mathbb{C}^{M_i N_i J_i \times K}$  denotes directional matrix of the  $i$ -th subarray and is presented by the following:

$$\mathbf{A}_i = \begin{bmatrix} \mathbf{a}_{x,i}(u_1) \otimes \mathbf{a}_{y,i}(v_1) \otimes \mathbf{a}_{z,i}(w_1), \dots, \mathbf{a}_{x,i}(u_K) \otimes \mathbf{a}_{y,i}(v_K) \\ \otimes \mathbf{a}_{z,i}(w_K) \end{bmatrix}, \quad (8)$$

where  $\mathbf{a}_{x,i}(u_k) = [1, e^{j2\pi d_{x,i} u_k / \lambda}, \dots, e^{j2\pi (M_i - 1) d_{x,i} u_k / \lambda}]^T$ ,  $\mathbf{a}_{y,i}(v_k) = [1, e^{j2\pi d_{y,i} v_k / \lambda}, \dots, e^{j2\pi (N_i - 1) d_{y,i} v_k / \lambda}]^T$  and  $\mathbf{a}_{z,i}(w_k) = [1, e^{j2\pi d_{z,i} w_k / \lambda}, \dots, e^{j2\pi (J_i - 1) d_{z,i} w_k / \lambda}]^T$  ( $k = 1, 2, \dots, K$ ) correspond to steering vectors of  $x$ -axis,  $y$ -axis, and  $z$ -axis of the subarray  $i$ .

Denote the directional matrix in (7) as follows:

$$\begin{aligned} \mathbf{A}_i &= \mathbf{A}_{x,i} \odot \mathbf{A}_{y,i} \odot \mathbf{A}_{z,i} \\ &= \begin{bmatrix} \mathbf{A}_{z,i} \mathbf{D}_1(\mathbf{A}_{y,i}) \mathbf{D}_1(\mathbf{A}_{x,i}) \\ \mathbf{A}_{z,i} \mathbf{D}_1(\mathbf{A}_{y,i}) \mathbf{D}_2(\mathbf{A}_{x,i}) \\ \vdots \\ \mathbf{A}_{z,i} \mathbf{D}_{N_i}(\mathbf{A}_{y,i}) \mathbf{D}_{M_i}(\mathbf{A}_{x,i}) \end{bmatrix}, \end{aligned} \quad (9)$$

where  $\mathbf{A}_{x,i}$  denotes directional matrix of  $x$ -axis of the subarray  $i$ , and  $\mathbf{A}_{y,i}, \mathbf{A}_{z,i}$  stand for the matrices of  $y$ -axis and  $z$ -axis, respectively,  $\mathbf{D}_{n_i}(\mathbf{A}_{y,i})$  ( $n = 1, 2, \dots, N$  and  $i = 1, 2$ ) denotes a diagonal matrix which is formed of the  $n$ -th row of the matrix  $\mathbf{A}_{y,i}$  for the subarray  $i$ , and  $\mathbf{D}_{m_i}(\mathbf{A}_{x,i})$  ( $m = 1, 2, \dots, M$  and  $i = 1, 2$ ) denotes a diagonal matrix which is formed of the  $m$ -th row of the matrix  $\mathbf{A}_{x,i}$  for the subarray  $i$ .

### 3. 2D DOA Estimation Algorithm

Conventional MD-MUSIC algorithm can obtain DOA estimates with high accuracy by selecting a refined search step, which causes expensive computational complexity. To tackle the problems, an AMRD-MUSIC algorithm is proposed.

3.1. MD-MUSIC Spectrum. We concatenate the array measurements  $\mathbf{x}_1(t)$  and  $\mathbf{x}_2(t)$  as follows:

$$\begin{aligned} \mathbf{x}(t) &= \begin{bmatrix} \mathbf{x}_1(t) \\ \mathbf{x}_2(t) \end{bmatrix} = \begin{bmatrix} \mathbf{A}_1 \\ \mathbf{A}_2 \end{bmatrix} \mathbf{s}(t) + \begin{bmatrix} \mathbf{n}_1(t) \\ \mathbf{n}_2(t) \end{bmatrix} \\ &= \mathbf{A} \mathbf{s}(t) + \mathbf{n}(t), \end{aligned} \quad (10)$$

where  $\mathbf{A} = [\mathbf{A}_1^T, \mathbf{A}_2^T]^T$  and  $\mathbf{n}(t) = [\mathbf{n}_1^T(t), \mathbf{n}_2^T(t)]^T$ .  $\mathbf{A}_1 \in \mathbb{C}^{M_1 N_1 J_1 \times K}$  and  $\mathbf{A}_2 \in \mathbb{C}^{M_2 N_2 J_2 \times K}$ . Then, the covariance matrix of the total array can be computed by the following:

$$\hat{R} = \frac{1}{L} \sum_{t=1}^L \mathbf{x}(t)\mathbf{x}^H(t) = \mathbf{U}_s \boldsymbol{\Sigma}_s \mathbf{U}_s^H + \mathbf{U}_n \boldsymbol{\Sigma}_n \mathbf{U}_n^H, \quad (11)$$

where  $\mathbf{U}_n \in \mathbb{C}^{(M_1 N_1 J_1 + M_2 N_2 J_2) \times (M_1 N_1 J_1 + M_2 N_2 J_2 - K)}$  refers to noise subspace and  $\mathbf{U}_s \in \mathbb{C}^{(M_1 N_1 J_1 + M_2 N_2 J_2) \times K}$  signifies signal subspace.  $\boldsymbol{\Sigma}_s \in \mathbb{C}^{K \times K}$  is a diagonal matrix with the  $K$  largest eigenvalues of  $\hat{R}$  and  $\boldsymbol{\Sigma}_n$  contains the remaining eigenvalues. Here, the symbol of  $(\hat{\cdot})$  means the estimation of the covariance matrix  $\mathbf{R}$ .

Then, according to 1D MUSIC spectrum [12], the MD-MUSIC spectrum can be solved as follows:

$$\begin{aligned} f(u, v, w) &= \frac{1}{\mathbf{a}^H(u, v, w) \mathbf{U}_n \mathbf{U}_n^H \mathbf{a}(u, v, w)} \\ &= \frac{1}{[\mathbf{a}_1^H(u, v, w) \mathbf{a}_2^H(u, v, w)] \mathbf{U}_n \mathbf{U}_n^H \begin{bmatrix} \mathbf{a}_1(u, v, w) \\ \mathbf{a}_2(u, v, w) \end{bmatrix}} \end{aligned} \quad (12)$$

**3.2. Array Mapping.** In this subsection, we utilize array mapping to extract two uniform arrays from the nonuniform array by exploiting the relation derived from the signal subspace and the two directional submatrices.

As the signal subspace spans the same space with the steering matrix doing, we have

$$\mathbf{U}_s = \begin{bmatrix} \mathbf{A}_1 \\ \mathbf{A}_2 \end{bmatrix} \mathbf{T}, \quad (13)$$

where  $\mathbf{T} \in \mathbb{C}^{K \times K}$  represents a nonsingular matrix. Then, the signal subspace can be decomposed into two parts:

$$\mathbf{U}_s = \begin{bmatrix} \mathbf{U}_{s1} \\ \mathbf{U}_{s2} \end{bmatrix} = \begin{bmatrix} \mathbf{A}_1 \\ \mathbf{A}_2 \end{bmatrix} \mathbf{T}, \quad (14)$$

where  $\mathbf{U}_{s1} \in \mathbb{C}^{M_1 N_1 J_1 \times K}$  and  $\mathbf{U}_{s2} \in \mathbb{C}^{M_2 N_2 J_2 \times K}$ .

Then, the transformation matrices can be defined as follows [38]:

$$\begin{aligned} \mathbf{H}_1 &= \mathbf{U}_{s2} \mathbf{U}_{s1}^+ = \mathbf{A}_2 \mathbf{T} \mathbf{T}^{-1} \mathbf{A}_1^+ = \mathbf{A}_2 \mathbf{A}_1^+, \\ \mathbf{H}_2 &= \mathbf{U}_{s1} \mathbf{U}_{s2}^+ = \mathbf{A}_1 \mathbf{T} \mathbf{T}^{-1} \mathbf{A}_2^+ = \mathbf{A}_1 \mathbf{A}_2^+, \end{aligned} \quad (15)$$

where  $(\cdot)^+$  denotes the pseudoinverse operation. From (15), we have the following:

$$\begin{aligned} \mathbf{A}_2 &= \mathbf{H}_1 \mathbf{A}_1, \\ \mathbf{A}_1 &= \mathbf{H}_2 \mathbf{A}_2, \end{aligned} \quad (16)$$

and the steering vectors of  $\mathbf{a}_1(u, v, w)$  and  $\mathbf{a}_2(u, v, w)$  also satisfy this relation in (16), so we have the following:

$$\begin{aligned} \mathbf{a}_2(u, v, w) &= \mathbf{H}_1 \mathbf{a}_1(u, v, w), \\ \mathbf{a}_1(u, v, w) &= \mathbf{H}_2 \mathbf{a}_2(u, v, w). \end{aligned} \quad (17)$$

By utilizing (17), we transform (13) into the following:

$$\begin{aligned} f_1(u, v, w) &= \frac{1}{[\mathbf{a}_1^H(u, v, w) \mathbf{a}_1^H(u, v, w) \mathbf{H}_1^H] \mathbf{U}_n \mathbf{U}_n^H \begin{bmatrix} \mathbf{a}_1(u, v, w) \\ \mathbf{H}_1 \mathbf{a}_1(u, v, w) \end{bmatrix}} \end{aligned} \quad (18)$$

$$\begin{aligned} &= \frac{1}{\mathbf{a}_1^H(u, v, w) \prod_1 \prod_1^H \mathbf{a}_1(u, v, w)}, \\ f_2(u, v, w) &= \frac{1}{[\mathbf{a}_2^H(u, v, w) \mathbf{H}_2^H \mathbf{a}_2^H(u, v, w)] \mathbf{U}_n \mathbf{U}_n^H \begin{bmatrix} \mathbf{H}_2 \mathbf{a}_2(u, v, w) \\ \mathbf{a}_2(u, v, w) \end{bmatrix}} \\ &= \frac{1}{\mathbf{a}_2^H(u, v, w) \prod_2 \prod_2^H \mathbf{a}_2(u, v, w)}, \end{aligned} \quad (19)$$

where  $\prod_1 = [\mathbf{I}_{M_1 N_1 J_1} \quad \mathbf{H}_1^H] \mathbf{U}_n$  and  $\prod_2 = [\mathbf{H}_2^H \quad \mathbf{I}_{M_2 N_2 J_2}] \mathbf{U}_n$ .

**3.3. Reduced Dimension Processing.** In this part, we employ the double reduced dimension processing on (16) and (17), respectively, to transform the 2D SPS into 1D one. Therefore, the computational complexity can be significantly reduced.

As  $\mathbf{a}_i(u, v, w) = \mathbf{a}_{x,i}(u) \otimes \mathbf{a}_{y,i}(v) \otimes \mathbf{a}_{z,i}(w) = \mathbf{a}_{x,i}(u) \otimes (\mathbf{a}_{y,i}(v) \otimes \mathbf{a}_{z,i}(w)) = (\mathbf{a}_{x,i}(u) \otimes \mathbf{I}_{N_i J_i}) (\mathbf{a}_{y,i}(v) \otimes \mathbf{a}_{z,i}(w))$ , then we have

$$\mathbf{a}_1(u, v, w) = (\mathbf{a}_{x,1}(u) \otimes \mathbf{I}_{N_1 J_1}) (\mathbf{a}_{y,1}(v) \otimes \mathbf{a}_{z,1}(w)), \quad (20)$$

$$\mathbf{a}_2(u, v, w) = (\mathbf{a}_{x,2}(u) \otimes \mathbf{I}_{N_2 J_2}) (\mathbf{a}_{y,2}(v) \otimes \mathbf{a}_{z,2}(w)), \quad (21)$$

where  $\mathbf{I}_{N_1 J_1}$  and  $\mathbf{I}_{N_2 J_2}$  are both identity matrices.

Then, we define the function  $\mathbf{Q}_i(u, v, w)$  ( $i = 1, 2$ ) as follows:

$$\mathbf{Q}_i(u, v, w) = \mathbf{a}_i^H(u, v, w) \prod_i \prod_i^H \mathbf{a}_i(u, v, w), \quad (22)$$

which transforms the 2D SPS to find the minimum value of (22). According to (20) and (21), we have the following:

$$\begin{aligned}
\mathbf{Q}_i(u, v, w) &= (\mathbf{a}_{x,i}(u) \otimes \mathbf{a}_{y,i}(v) \otimes \mathbf{a}_{z,i}(w))^H \prod_i \prod_i^H (\mathbf{a}_{x,i}(u) \otimes \mathbf{a}_{y,i}(v) \otimes \mathbf{a}_{z,i}(w)) \\
&= (\mathbf{a}_{x,i}(u) \otimes \mathbf{I}_{N_i J_i}) (\mathbf{a}_{y,i}(v) \otimes \mathbf{a}_{z,i}(w))^H \prod_i \prod_i^H ((\mathbf{a}_{x,i}(u) \otimes \mathbf{I}_{N_i J_i}) (\mathbf{a}_{y,i}(v) \otimes \mathbf{a}_{z,i}(w)))^H \\
&= (\mathbf{a}_{y,i}(v) \otimes \mathbf{a}_{z,i}(w))^H (\mathbf{a}_{x,i}(u) \otimes \mathbf{I}_{N_i J_i})^H \prod_i \prod_i^H (\mathbf{a}_{x,i}(u) \otimes \mathbf{I}_{N_i J_i}) (\mathbf{a}_{y,i}(v) \otimes \mathbf{a}_{z,i}(w)) \\
&= (\mathbf{a}_{y,i}(v) \otimes \mathbf{a}_{z,i}(w))^H \mathbf{G}_i(u) (\mathbf{a}_{y,i}(v) \otimes \mathbf{a}_{z,i}(w)) \\
&= \mathbf{f}_i^H(v, w) \mathbf{G}_i(u) \mathbf{f}_i(v, w),
\end{aligned} \tag{23}$$

where  $\mathbf{G}_i(u) = (\mathbf{a}_{x,i}(u) \otimes \mathbf{I}_{N_i J_i})^H \prod_i \prod_i^H (\mathbf{a}_{x,i}(u) \otimes \mathbf{I}_{N_i J_i})$ ,  $\mathbf{f}_i(v, w) = \mathbf{a}_{y,i}(v) \otimes \mathbf{a}_{z,i}(w)$ , and  $\mathbf{f}_i(v, w) \in \mathbb{C}^{N_i J_i \times 1}$ . Note that (23) is an optimization problem. Based on  $\mathbf{e}^H \mathbf{f}_i^H(v, w) = 1$ , where  $\mathbf{e} = [1, 0, \dots, 0]^T \in \mathbb{C}^{N_i J_i}$ , we can eliminate the trivial solution  $\mathbf{f}_i^H(v, w) = 0$ . This optimization problem can be reconstructed as follows:

$$\begin{aligned}
\min_{(u,v,w)} \quad & \mathbf{f}_i^H(v, w) \mathbf{G}_i(u) \mathbf{f}_i(v, w) \\
\text{s.t.} \quad & \mathbf{e}^H \mathbf{f}_i^H(v, w) = 1.
\end{aligned} \tag{24}$$

Then, we can construct the cost function as follows:

$$L(u, v, w) = \mathbf{f}_i^H(v, w) \mathbf{G}_i(u) \mathbf{f}_i(v, w) - \lambda (\mathbf{e}^H \mathbf{f}_i^H(v, w) - 1), \tag{25}$$

where  $\lambda$  is a constant. Then, we have the following:

$$\frac{\partial}{\partial \mathbf{f}(v, w)} L(u, v, w) = 2 \mathbf{G}_i(u) \mathbf{f}_i(v, w) + \lambda \mathbf{e}. \tag{26}$$

According to (26), we have  $\mathbf{f}_i(v, w) = \xi \mathbf{G}_i^{-1}(u) \mathbf{e}$ , where  $\xi$  is a constant. Combining (24), we have the following:

$$\xi = \frac{1}{\mathbf{e}^H \mathbf{G}_i^{-1}(u) \mathbf{e}}. \tag{27}$$

Then,  $\mathbf{f}_i(v, w)$  can be denoted as follows:

$$\mathbf{f}_i(v, w) = \frac{\mathbf{G}_i^{-1}(u) \mathbf{e}}{\mathbf{e}^H \mathbf{G}_i^{-1}(u) \mathbf{e}}. \tag{28}$$

Based on (24) and (28), we can obtain the following:

$$\hat{u}_k = \arg \min_u \frac{1}{\mathbf{e}^H \mathbf{G}_i^{-1}(u) \mathbf{e}} = \arg \max_u \mathbf{e}^H \mathbf{G}_i^{-1}(u) \mathbf{e}. \tag{29}$$

According to (29), the 2D SPS is transformed into 1D one by utilizing a reduced dimension process. To further reduce complexity, we employ the polynomial rooting technique with the lower computational complexity to obtain the final DOA estimates instead of the 1D SPS process.

**3.4. Polynomial Root Finding Process.** Define  $z_{x,i} = e^{-j2\pi d_i u / \lambda}$ , ( $i = 1, 2$ ) and denote  $\mathbf{a}_{x,i}(u)$  as follows:

$$\mathbf{a}_{x,i}(u) = \mathbf{a}(z_{x,i}) = [1, z_{x,i}, z_{x,i}^2, \dots, z_{x,i}^{M_i-1}]^T. \tag{30}$$

Then, we rewrite  $\mathbf{G}_i(u)$  as follows:

$$\mathbf{G}(z_{x,i}) = (\mathbf{a}^H(z_{x,i}) \otimes \mathbf{I}_{N_i J_i})^H \prod_i \prod_i^H (\mathbf{a}(z_{x,i}) \otimes \mathbf{I}_{N_i J_i}). \tag{31}$$

Then, we employ polynomial root finding technique instead of 1D SPS.

$$(\mathbf{a}^H(z_{x,i}) \otimes \mathbf{I}_{N_i J_i})^H \prod_i \prod_i^H (z_{x,i}) \prod_i^H (\mathbf{a}(z_{x,i}) \otimes \mathbf{I}_{N_i J_i}) = 0. \tag{32}$$

If  $z_{x,i}$  cannot match with one source signal and if

$$\text{Rank}(\prod_i) \geq N_i J_i, \tag{33}$$

the matrix  $\prod_i$  is invertible [38].

In order to achieve the polynomial (32),  $z_{x,i}$  satisfies

$$\mathbf{D}(z_{x,i}) = \det(\prod(z_{x,i})) = 0. \tag{34}$$

Then, we can obtain the final  $\hat{u}_i^{(k)}$  by finding  $K$  roots which are closest to the unit circle of the polynomial  $\mathbf{D}(z_{x,i})$ ,  $z_{x,i}^k |_{k=1,2,\dots,K}$ ,

$$\hat{u}_i^{(k)} = \text{angle}(z_{x,i}^{(k)}) \frac{\lambda}{2\pi d_i}. \tag{35}$$

In order to obtain the estimation of  $\hat{v}_i^{(k)}$  or  $\hat{w}_i^{(k)}$ , the similar reduced dimensional polynomial root finding technique can be employed again. We can reform the whole steering matrix as  $\mathbf{A}_i' = [\mathbf{a}_{y,i}(v_1) \otimes \mathbf{a}_{x,i}(u_1) \otimes \mathbf{a}_{z,i}(w_1), \dots, \mathbf{a}_{y,i}(v_K) \otimes \mathbf{a}_{x,i}(u_K) \otimes \mathbf{a}_{z,i}(w_K)]$ , which contains the same elements as the matrix  $\mathbf{A}_i$  and only differs in elements positions. Then, a reconstructed received signal can be obtained. Then, we operate the proposed array mapping, reduced dimension, and polynomial rooting technique again to attain the estimate of  $\hat{v}_i^{(k)}$

$$\hat{v}_i^{(k)} = \text{angle}(z_{y,i}^{(k)}) \frac{\lambda}{2\pi d_i}. \tag{36}$$

Similarly, we can achieve  $\hat{w}_i^{(k)}$ . Phase ambiguity problem, resulting from the larger element spacing than half-wavelength, will be solved by coprime property in the following section.

**3.5. Ambiguity Elimination.** Firstly, the phase ambiguity problem is illustrated. Then, the coprime property is exploited to tackle the problem.

Assume that only one signal located with  $(\theta_\tau, \phi_\tau)$  impinges on the CCA subarray and the subarray consists of  $M_i \times N_i \times J_i$  sensors.  $(\theta_a, \phi_a)$  is assumed as one of the ambiguous DOAs of the real angle  $(\theta_\tau, \phi_\tau)$ .

According to [38],

$$\begin{cases} \text{mod}\left(\frac{2\pi}{\lambda}d_{xi}u_\tau\right) + 2k_u\pi = \frac{2\pi}{\lambda}d_{xi}u_\tau, \\ \text{mod}\left(\frac{2\pi}{\lambda}d_{yi}v_\tau\right) + 2k_v\pi = \frac{2\pi}{\lambda}d_{yi}v_\tau, \\ \text{mod}\left(\frac{2\pi}{\lambda}d_{zi}w_\tau\right) + 2k_w\pi = \frac{2\pi}{\lambda}d_{zi}w_\tau, \end{cases} \quad (37)$$

where the mod operation depends on the period of the exponential function  $2\pi$ . So it can be noted that the phase difference between the real and ambiguous DOAs is  $2k\pi$  ( $k \in \mathbb{Z}$ ) [39] and  $k_u, k_v, k_w \in \mathbb{Z}$  are integers. And  $d_{xi} = N_j\lambda/2$ ,  $d_{yi} = M_j\lambda/2$ ,  $d_{zi} = J_j\lambda/2$  ( $i, j \in [1, 2], i \neq j$ ) denote the element spacing among three axes, respectively.  $u_\tau = \sin \theta_\tau \cos \phi_\tau, v_\tau = \sin \theta_\tau \sin \phi_\tau, w_\tau = \cos \theta_\tau$ .

Then, we employ the obtained estimates to recover all estimates [28],

$$\frac{2\pi d_{xi}(u_\tau - u_a)}{\lambda} = 2k_u\pi, \quad (38)$$

$$\frac{2\pi d_{yi}(v_\tau - v_a)}{\lambda} = 2k_v\pi, \quad (39)$$

$$\frac{2\pi d_{zi}(w_\tau - w_a)}{\lambda} = 2k_w\pi, \quad (40)$$

where  $u_a = \sin \theta_a \cos \phi_a$ ,  $v_a = \sin \theta_a \sin \phi_a$ , and  $w_a = \cos \theta_a$  are defined and they denote the ambiguous values.

As  $\theta \in (0, \pi/2)$  and  $\phi \in (0, \pi)$ , we have  $u_a \in (-1, 1)$ ,  $v_a \in (0, 1)$ ,  $w_a \in (0, 1)$ . Simultaneously,  $u_a^2 + v_a^2 \in (0, 1)$  and  $u_a^2 + v_a^2 + w_a^2 = 1$  demand to satisfy each estimate.

As the interelement spacing of conventional UCA is limited to half-wavelength,  $k_u, k_v, k_w$  can only be the value of zero, which means no ambiguity problem exists. However, in CCA, due to the interelement spacing larger than half-wavelength, there are other pairs to make (37)–(39) hold besides the infeasible  $k_u, k_v$ , and  $k_w$  pairs, whereas only one pair is the candidate related to the actual DOA. Coprime property is utilized to solve the phase ambiguity problem and achieve true DOA.

Assume  $(\theta_a, \phi_a)$  as one of the ambiguous DOAs that appears in one of the subarrays. Simultaneously, define  $(\theta_i, \phi_i)$  as the corresponding actual DOA. There exists the following:

$$u_\tau - u_a = \frac{2k_{ui}}{M_j},$$

$$v_\tau - v_a = \frac{2k_{vi}}{N_j}, \quad (41)$$

$$w_\tau - w_a = \frac{2k_{wi}}{J_j}.$$

It exists that  $k_{ui} \in (-M_j, M_j)$ ,  $k_{vi} \in (-N_j/2, N_j/2)$ ,  $k_{wi} \in (-J_j/2, J_j/2)$ ,  $i, j \in \{1, 2\}, i \neq j$  [38], so we can obtain

$$\begin{aligned} \frac{k_{u1}}{M_2} &= \frac{k_{u2}}{M_1}, \\ \frac{k_{v1}}{N_2} &= \frac{k_{v2}}{N_1}, \\ \frac{k_{w1}}{J_2} &= \frac{k_{w2}}{J_1}. \end{aligned} \quad (42)$$

Since  $N_1, N_2, M_1, M_2$  and  $J_1, J_2$  are coprime integers pairs, respectively, (41) can hold only in the case of  $k_{u1} = k_{u2} = 0$ ,  $k_{v1} = k_{v2} = 0$ ,  $k_{w1} = k_{w2} = 0$ . It is indicated that the ambiguity problem is solved and actual DOA estimates can be achieved.

In practice, we only need two variables of  $(\hat{u}_k, \hat{v}_k, \hat{\gamma}_k)$  to achieve DOAs  $(\theta_k, \phi_k)$  estimates, where  $\hat{u}_k, \hat{v}_k, \hat{\gamma}_k$  are the estimates of  $u_k, v_k, \gamma_k$  ( $k = 1, 2, \dots, K$ ).

The final estimate of  $(\theta_k, \phi_k)$  can be calculated by the following:

$$\begin{aligned} \hat{\theta}_k &= \frac{\arcsin \sqrt{\hat{u}_k^2 + \hat{v}_k^2} + \arccos \hat{w}_k}{2}, \\ \hat{\phi}_k &= \frac{\arctan(\hat{u}_k/\hat{v}_k) + \arccos(\hat{u}_k/\sqrt{1 - \hat{w}_k^2})}{2}. \end{aligned} \quad (43)$$

**3.6. Detailed Steps of the Proposed Algorithm.** The steps are provided in detail as follows:

Step 1: compute the covariance of the received signal data to obtain the MD-MUSIC spectrum function (12).

Step 2: according to the signal subspace, construct  $\hat{H}_1$  and  $\hat{H}_2$  by (15), with which we can obtain the reconstructed spectrum function according to (19).

Step 3: by array mapping, we extract the two uniform arrays (19) from the nonuniform array (12) according to the relation derived from two directional matrices.

Step 4: according to (20) and (21), transform the 2D SPS process into 1D SPS.

Step 5: according to (32), convert 1D PSS to polynomial root finding process and obtain the  $K$  roots of  $\hat{u}_i^{(k)}$ . Similarly, we can achieve  $\hat{v}_i^{(k)}$  and  $\hat{w}_i^{(k)}$ .

Step 6: by (41), all the ambiguous DOA estimates are recovered, and by searching for the nearest ones, the actual estimations of  $u^{(k)}$ ,  $v^{(k)}$  and  $w^{(k)}$  can be achieved.

Step 7: according to (43), the final DOAs estimates can be obtained.

#### 4. Performance Analysis of the Algorithm

**4.1. DOF Comparison.** The proposed AMRD-MUSIC algorithm can obtain  $M_1N_1J_1 + M_2N_2J_2 - 1$  DOFs, which indicates that the proposed algorithm can achieve  $M_1N_1J_1 + M_2N_2J_2 - 2$  signals by employing  $M_1N_1J_1 + M_2N_2J_2 - 1$  antennas.

$$\text{DOF}_{\text{CCA}}^{\text{AMRD-MUSIC}} = M_1N_1J_1 + M_2N_2J_2 - 1. \quad (44)$$

The algorithms in [24, 26] process the two subarrays separately so that they have a great loss in DOFs since they only exploit the autoinformation. The number of achievable DOFs by using the method in [24, 26] can be denoted as follows:

$$\text{DOF}_{\text{CCA}}^{\text{algorithms in [24,26]}} = \min(M_1N_1J_1, M_2N_2J_2), \quad (45)$$

where  $M_1 = N_1 = J_1 > M_2 = N_2 = J_2$ .

Thus, the proposed algorithms can detect many more signals than conventional algorithms with the same sensors. From (44) and (45), we can note the relationship of DOFs of different algorithms as follows:

$$\text{DOF}_{\text{CCA}}^{\text{algorithms in [24,26]}} < \text{DOF}_{\text{CCA}}^{\text{AMRD-MUSIC}}. \quad (46)$$

Figure 2 depicts the maximum number of achievable DOFs to illustrate the signals explicitly without ambiguous DOA estimations, where the number of snapshots is set to be  $L = 500$  with noise-free, the total number of signals is  $K = 28$ , and the total number of sensors is  $T = 3 \times 2 \times 3 + 2 \times 3 \times 2 - 1 = 29$ . The elevation angles and azimuth angles are set to be  $\theta = [20^\circ, 20^\circ, 20^\circ, 20^\circ, 20^\circ, 20^\circ, 20^\circ, 20^\circ, 40^\circ, 40^\circ, 40^\circ, 40^\circ, 40^\circ, 40^\circ, 40^\circ, 60^\circ, 60^\circ, 60^\circ, 60^\circ, 60^\circ, 60^\circ, 60^\circ, 60^\circ, 80^\circ, 80^\circ, 80^\circ, 80^\circ, 80^\circ, 80^\circ]$  and  $\phi = [15^\circ, 25^\circ, 35^\circ, 45^\circ, 55^\circ, 65^\circ, 75^\circ, 15^\circ, 25^\circ, 35^\circ, 45^\circ, 55^\circ, 65^\circ, 75^\circ, 15^\circ, 25^\circ, 35^\circ, 45^\circ, 55^\circ, 65^\circ, 75^\circ, 15^\circ, 25^\circ, 35^\circ, 45^\circ, 55^\circ, 65^\circ, 75^\circ]$  respectively. From Figure 2, we can obviously see that the 28 signals can be detected uniquely due to the employment of total correlation matrix information including autocorrelation matrix and mutual correlation matrix, where no ambiguous angles arise; however, the methods in [24, 26] fail to detect 28 signals and they can detect 11 signals at most in this scenario.

**4.2. Complexity Analysis.** In this subsection, we compute the complexity of the classical MD-MUSIC algorithm, multiple-dimensional ESPRIT (MD-ESPRIT) algorithm and the proposed AMRD-MUSIC algorithm for the same array configuration of CCA with the same sensors.

For the MD-MUSIC algorithm, the total complexity is composed of three parts, including computing covariance, eigenvalues decomposition, and spectrum peak searching. The complexity of these three parts is presented as  $T^2L$ ,  $T^3$  and  $(180/\tau)(90/\tau)[T(T-K)]$ , respectively, where  $L$

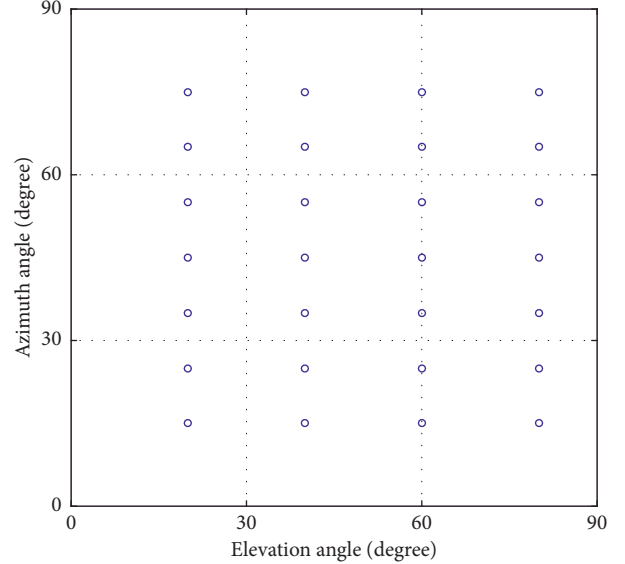


FIGURE 2: Maximum achievable DOFs without ambiguous angles by using the AMRD-MUSIC algorithm.

represents the number of snapshots  $T = T_1 + T_2$ ,  $T_1 = M_1N_1J_1$ ,  $T_2 = M_2N_2J_2$  and  $\tau$  denotes the searching step. So the total computational complexity can be denoted as  $T^2L + T^3 + (180/\tau)(90/\tau)[T(T-K)]$ .

And we compute the complexity of the MD-ESPRIT algorithm. For the two subarrays, complexity consists of three parts, computing the covariance as  $T^2L$ , eigenvalue decomposition as  $T_1^3 + T_2^3$ , computing pseudoinverse and eigenvalue decomposition after reconstruction as  $(T_1 - N_1J_1)^3 + (T_2 - N_2J_2)^3 + (T_1 - M_1J_1)^3 + (T_2 - M_2J_2)^3 + (T_1 - N_1M_1)^3 + (T_2 - N_2M_2)^3$ . So the total complexity of these operations is denoted as  $T^2L + T_1^3 + T_2^3 + (T_1 - N_1J_1)^3 + (T_2 - N_2J_2)^3 + (T_1 - M_1J_1)^3 + (T_2 - M_2J_2)^3 + (T_1 - N_1M_1)^3 + (T_2 - N_2M_2)^3$ .

In the proposed AMRD-MUSIC algorithm, the complexity can be denoted as  $T_1^2L + 2KT_1T_2 + 2T_1T_2^2 + 2N_1J_1T_1T + (N_1J_1)^2T_1 + (T - N_1J)^3 + 2N_2J_2T_2T + (N_2J_2)^2T_2 + T_2^3$ , and the complexity of the other subarray is approximately similar to it.

We compare the complexity of the conventional MD-MUSIC algorithm, the MD-ESPRIT algorithm, and the proposed AMRD-MUSIC algorithm with the same CCA configuration. For clarity, we list the computational complexity of these algorithms with CCA in Table 2 with  $L = 200$ ,  $K = 2$ ,  $M_1 = 3$ ,  $M_2 = 2$ ,  $N_1 = 2$ ,  $N_2 = 3$ ,  $J_1 = 3$ ,  $J_2 = 2$ ,  $J_1 = 3$ ,  $J_2 = 2$ , and the searching step  $\tau$  is set to be 0.02.

We compare the computational complexity versus the number of snapshots and sensors respectively of three algorithms including MD-MUSIC, MD-ESPRIT, and ARMD-MUSIC. Figures 3 and 4 show the complexity comparison with the increasing number of snapshots and sensors, respectively. It can be seen that the proposed AMRD-MUSIC algorithm achieves the lowest computational complexity than other algorithms. Figure 5 shows the complexity comparison versus the searching step. We can see that the complexity of MD-MUSIC reduces with the searching step

TABLE 2: Computational complexity of different algorithms.

Algorithms	Complex multiplication
MD-MUSIC	$5.4432 \times 10^9$
MD-ESPRIT	$1.9212 \times 10^5$
AMRD-MUSIC	$1.20096 \times 10^5$

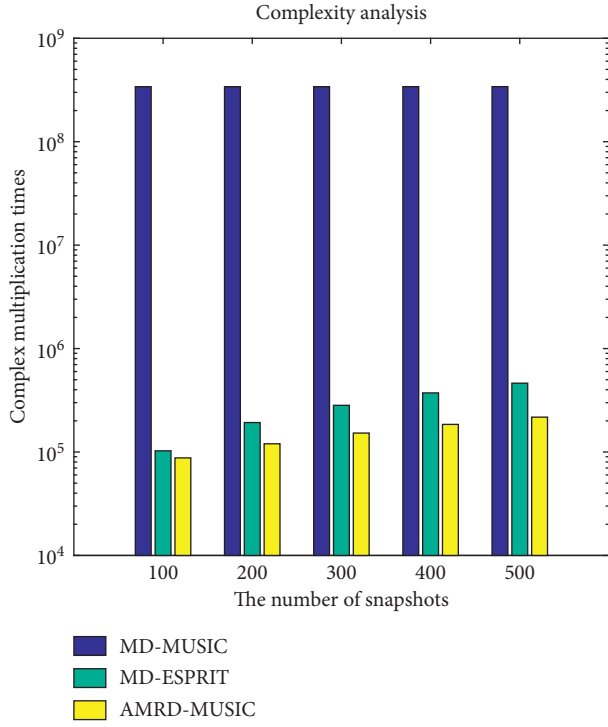


FIGURE 3: Comparison of total complexity versus snapshots.

increasing. However, the proposed AMRD-MUSIC algorithm outperforms the other algorithms.

4.3. *Advantages of the Proposed Algorithm.* In summary, the advantages of the proposed algorithm are listed as follows:

- (1) The proposed algorithm achieves significant complexity decrease by reducing 2D SPS into 1D one and utilizing polynomial root finding technique instead of 1D SPS.
- (2) The proposed algorithm possesses approximately the same DOA estimation performance as the MD-MUSIC algorithm and behaves better in its estimation than the classic MD-ESPRIT algorithm.
- (3) The proposed algorithm can obtain full DOFs due to the utilization of the total matrix information.
- (4) The proposed algorithm can achieve DOA angles with pairing automatically.

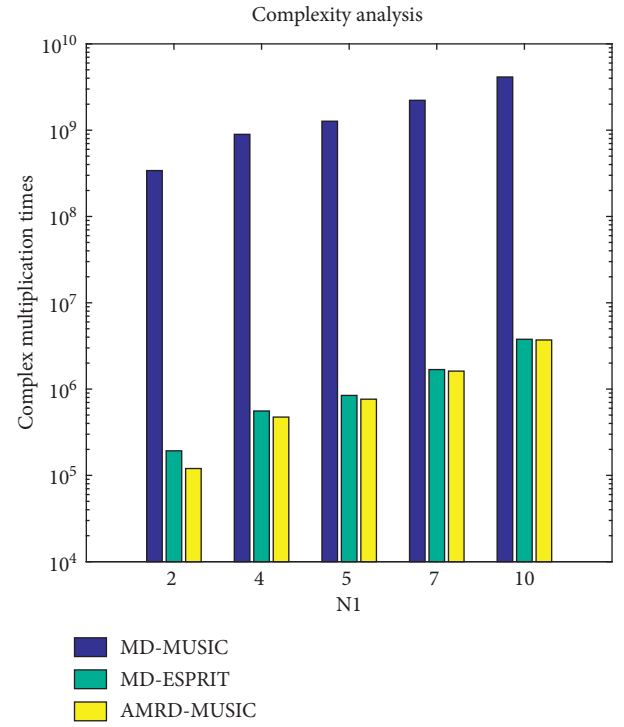


FIGURE 4: Comparison of total complexity versus the number of elements.

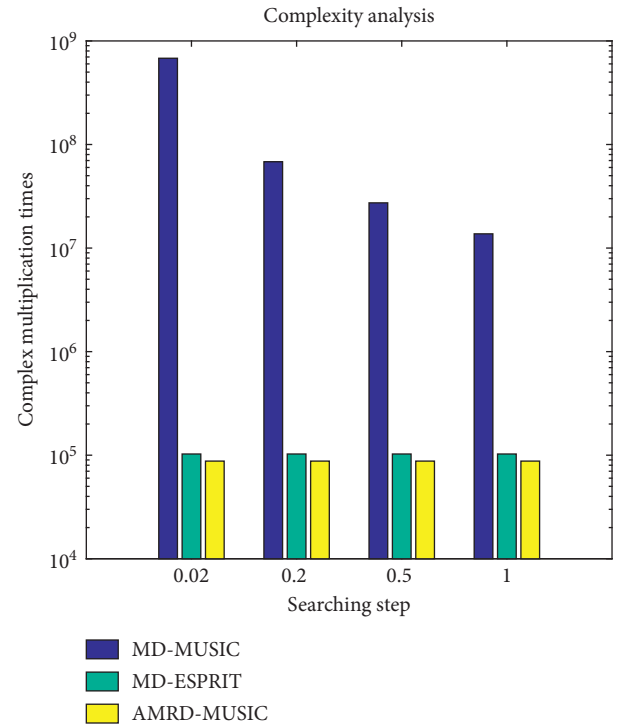


FIGURE 5: Comparison of total complexity versus searching step.



**4.4. Cramer–Rao Bound.** We provide the Cramer–Rao Bound (CRB) [40–42] analytical derivation of DOA estimation for CCA. The signal covariance can be obtained by the following:

$$\mathbf{R}_s = \frac{1}{L} \sum_{t=1}^L \mathbf{s}(t)\mathbf{s}^H(t), \quad (47)$$

and we define the matrix parameter vector  $\boldsymbol{\eta} = [\theta_1, \theta_2, \dots, \theta_K, \phi_1, \phi_2, \dots, \phi_K]^T$ .

Then, we can denote the  $(\xi_0, \zeta_0)$ -th element of the Fisher information matrix (FIM) as follows [42]:

$$\begin{aligned} \text{FIM}_{(\xi_0, \zeta_0)} &= \varsigma_0 \text{tr} \left( \frac{\partial \bar{\mathbf{p}}}{\partial \eta_{\xi_0}} \mathbf{P}^{-1} \frac{\partial \bar{\mathbf{p}}}{\partial \eta_{\zeta_0}} \mathbf{P}^{-1} \right) \\ &= \varsigma_0 \left( \frac{\partial \bar{\mathbf{p}}}{\partial \eta_{\xi_0}} \right)^H (\mathbf{P}^T \otimes \mathbf{P})^{-1} \frac{\partial \bar{\mathbf{p}}}{\partial \eta_{\zeta_0}}, \end{aligned} \quad (48)$$

where

$$\varsigma_0 = M_1 N_1 J_1 + M_2 N_2 J_2, \quad (49)$$

$$\mathbf{P} = \mathbf{A} \mathbf{P}_s \mathbf{A}^H + \mathbf{I}_{\varsigma_0}, \quad (50)$$

$$\bar{\mathbf{p}} = \text{vec}(\mathbf{P}) = (\mathbf{A}^* \circ \mathbf{A}) \boldsymbol{\Xi} + \text{vec}(\mathbf{I}_{\varsigma_0}), \quad (51)$$

and we denote  $\partial \bar{\mathbf{p}} / \partial \boldsymbol{\eta} = [\partial \bar{\mathbf{p}} / \partial \theta_1, \partial \bar{\mathbf{p}} / \partial \theta_2, \dots, \partial \bar{\mathbf{p}} / \partial \theta_K, \partial \bar{\mathbf{p}} / \partial \phi_1, \partial \bar{\mathbf{p}} / \partial \phi_2, \dots, \partial \bar{\mathbf{p}} / \partial \phi_K]$ ; then we have the following:

$$\text{FIM} = \varsigma_0 \left( \frac{\partial \bar{\mathbf{p}}}{\partial \boldsymbol{\eta}} \right)^H (\mathbf{P}^T \otimes \mathbf{P})^{-1} \frac{\partial \bar{\mathbf{p}}}{\partial \boldsymbol{\eta}}. \quad (52)$$

By utilizing (52), we can calculate the following:

$$\frac{\partial \bar{\mathbf{p}}}{\partial \boldsymbol{\eta}} = [\mathbf{A}_{d1} \boldsymbol{\Pi}, \mathbf{A}_{d2} \boldsymbol{\Pi}], \quad (53)$$

where

$$\mathbf{A}_{d1} = (\mathbf{D}_1^* \circ \mathbf{A} + \mathbf{A}^* \circ \mathbf{D}_1),$$

$$\mathbf{A}_{d2} = (\mathbf{D}_2^* \circ \mathbf{A} + \mathbf{A}^* \circ \mathbf{D}_2),$$

$$\mathbf{D}_1 = \left[ \frac{\partial \mathbf{a}(u_1, v_1)}{\partial \theta_1}, \frac{\partial \mathbf{a}(u_2, v_2)}{\partial \theta_2}, \dots, \frac{\partial \mathbf{a}(u_K, v_K)}{\partial \theta_K} \right],$$

$$\mathbf{D}_2 = \left[ \frac{\partial \mathbf{a}(u_1, v_1)}{\partial \phi_1}, \frac{\partial \mathbf{a}(u_2, v_2)}{\partial \phi_2}, \dots, \frac{\partial \mathbf{a}(u_K, v_K)}{\partial \phi_K} \right],$$

$$\mathbf{a}(u_k, v_k) = \begin{bmatrix} \mathbf{a}_{x1}(u_k) \otimes \mathbf{a}_{y1}(v_k) \otimes \mathbf{a}_{z1}(w_k) \\ \mathbf{a}_{x2}(u_k) \otimes \mathbf{a}_{y2}(v_k) \otimes \mathbf{a}_{z2}(w_k) \end{bmatrix}, \quad k = 1, 2, \dots, K,$$

$$\boldsymbol{\Pi} = \text{diag}(\boldsymbol{\Xi}).$$

(54)

The matrix  $\mathbf{P}^T \otimes \mathbf{P}$  is positive definite since the  $\mathbf{P}$  in (50) is positive definite.

By letting

$$\mathbf{F} = (\mathbf{P}^T \otimes \mathbf{P})^{-1/2} \mathbf{A}_d \mathbf{R}_0, \quad (55)$$

the CRB can be obtained as follows:

$$\text{CRB} = \frac{1}{\varsigma_0} (\mathbf{F}^H \mathbf{F})^{-1}, \quad (56)$$

where  $\mathbf{A}_d = [\mathbf{A}_{d1}, \mathbf{A}_{d2}]$ ,  $\mathbf{R}_0 = \text{diag}(\mathbf{R}_s, \mathbf{R}_s)$ .

## 5. Simulation Results

Numerical simulations are provided to evaluate the performance of the proposed array configuration of CCA and algorithm in this part. For the CCA geometry, it consists of two uniform cubic subarrays of  $3 \times 2 \times 3$  and  $2 \times 3 \times 2$  sensors, where  $d_{x1} = 2\lambda/2$ ,  $d_{y1} = 3\lambda/2$ ,  $d_{z1} = 2\lambda/2$ ,  $d_{x2} = 3\lambda/2$ ,  $d_{y2} = 2\lambda/2$ , and  $d_{z2} = 3\lambda/2$ . The total number of these two subarrays is computed as  $T = 3 \times 2 \times 3 + 2 \times 3 \times 2 - 1 = 29$ . The UCA consists of  $3 \times 2 \times 5 = 30$  sensors. Assume  $K = 2$  signals impinging on the arrays from  $(\theta_1, \phi_1) = (20^\circ, 30^\circ)$  and  $(\theta_2, \phi_2) = (50^\circ, 70^\circ)$ . From Figure 6, we can clearly see that the AMRD-MUSIC algorithm is able to detect the DOA targets successfully.

The root mean square error (RMSE), as the performance metric of the DOA estimation, is defined as follows:

$$\text{RMSE} = \sqrt{\frac{1}{\text{PK}} \sum_{p=1}^P \sum_{k=1}^K \left( (\theta_k - \hat{\theta}_k^p)^2 + (\phi_k - \hat{\phi}_k^p)^2 \right)}, \quad (57)$$

where  $K$  is the number of sources.  $(\hat{\theta}_k^p, \hat{\phi}_k^p)$  ( $k = 1, 2, \dots, K$ ) are estimates of  $(\theta_k, \phi_k)$  of the  $p$ -th Monte Carlo trial, respectively. In this paper, we set  $P = 500$ .

**5.1. DOA Estimation Performance Comparison of Different Array Configurations with the Same Algorithm.** We employ simulations to illustrate the DOA estimation performance of UCA and CCA configurations by using the same algorithm, where  $K = 2$ ,  $(\theta_1, \phi_1) = [15^\circ, 30^\circ]$ ,  $(\theta_2, \phi_2) = [20^\circ, 40^\circ]$ .

Figures 7 and 8 exhibit the RMSE performance comparison between CCA and UCA by utilizing the same algorithm. It captures explicitly that the proposed AMRD-MUSIC algorithm with CCA possesses better DOA estimation performance because of the extended array aperture and less MC effects. And CRB comparison shows that CCA can obtain the lower bound of theoretical DOA estimation performance compared with UCA geometry.

**5.2. DOA Estimation Performance Comparison of Different Algorithms with the Same Array.** In this subsection, we compare the RMSE performance of different algorithms with the same array of CCA, including the proposed AMRD-MUSIC algorithm, conventional MD-MUSIC algorithm, and MD-ESPRIT algorithm.

Figures 9 and 10 present the 2D angle estimation comparisons versus SNR and  $L$ , respectively. The two figures clearly show that the proposed AMRD-MUSIC algorithm has approximately the same DOA estimation performance as the MD-MUSIC algorithm and

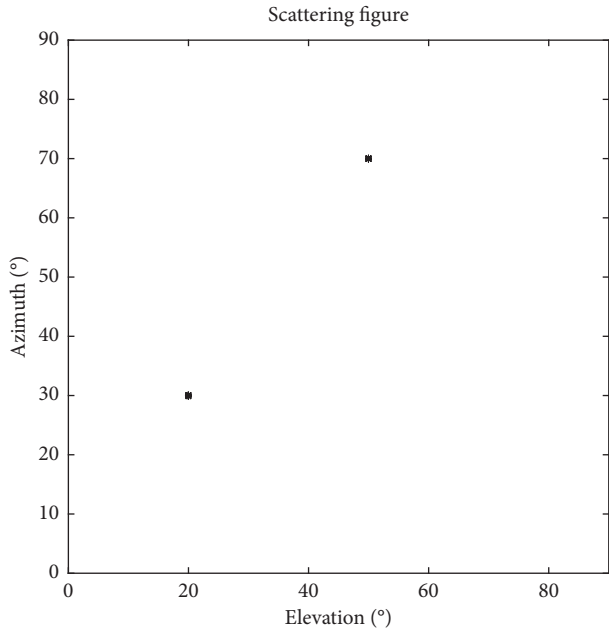


FIGURE 6: Scattering figure with AMRD-MUSIC for CCA.

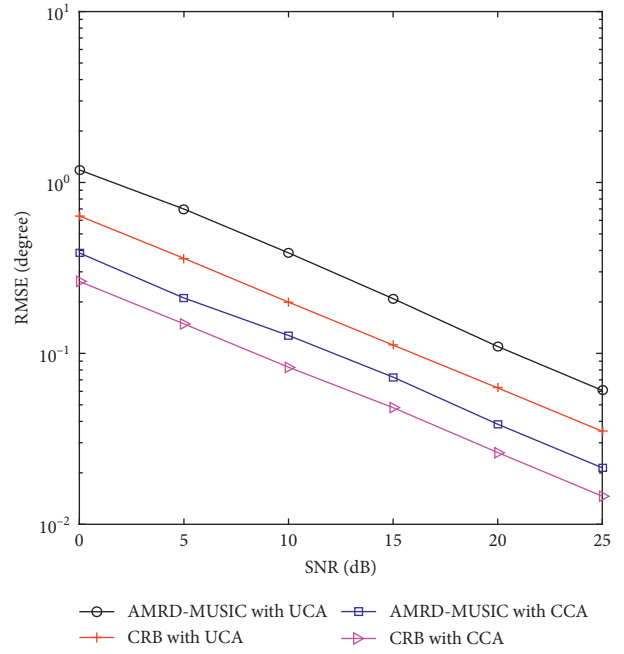


FIGURE 8: RMSE of different arrays versus SNR.

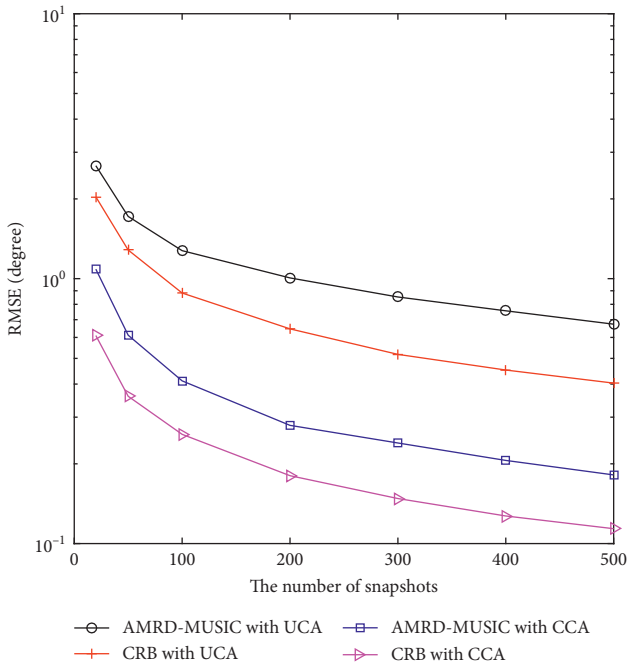


FIGURE 7: RMSE of different arrays versus snapshots.

outperforms the classic MD-ESPRIT algorithm owing to the utilization of total information including autocorrelation matrix and mutual correlation matrix, while the proposed algorithm has a lower computational complexity as shown in Figure 2.

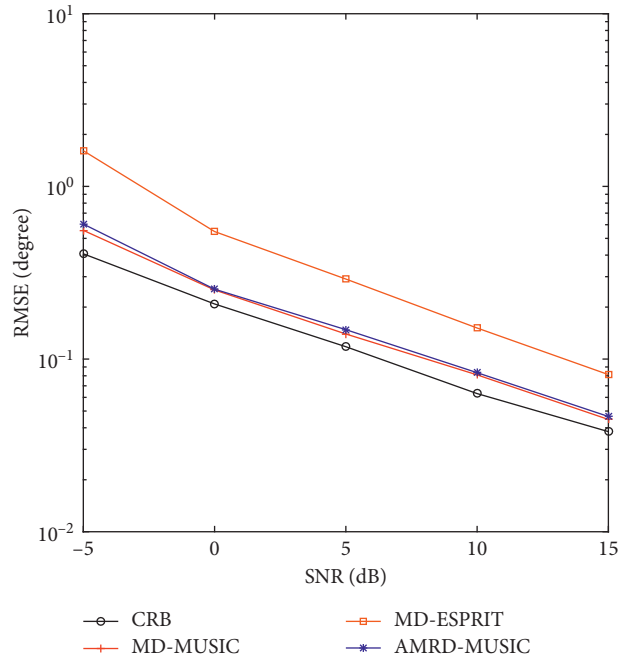


FIGURE 9: RMSE comparison of different algorithms versus SNR.

**5.3. Comparison of DOA Estimation Performance versus the Number of Sensors.** In this subsection, we employ the proposed approach to a CCA geometry which consists of two subarrays including  $3 \times N \times 3$  and  $2 \times 3 \times 2$  sensors, where  $N = [2, 4, 5]$ . The RMSE performance versus SNR and snapshots are displayed in Figures 11 and 12, respectively. It is

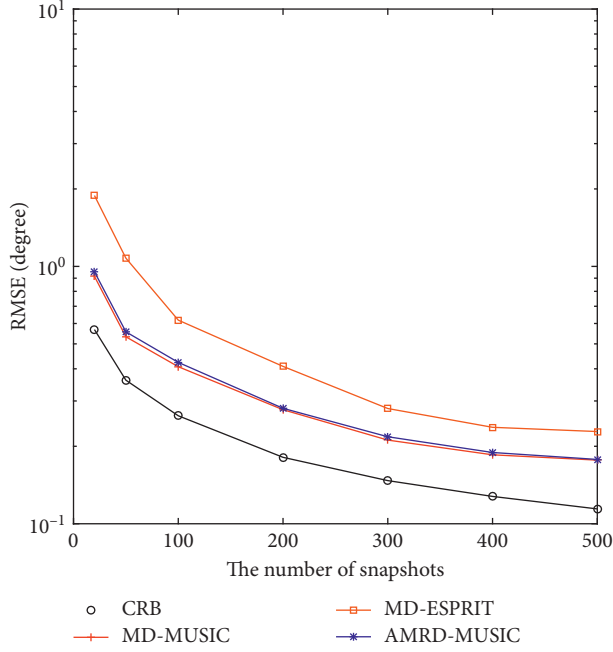


FIGURE 10: RMSE comparison of different algorithms versus snapshots.

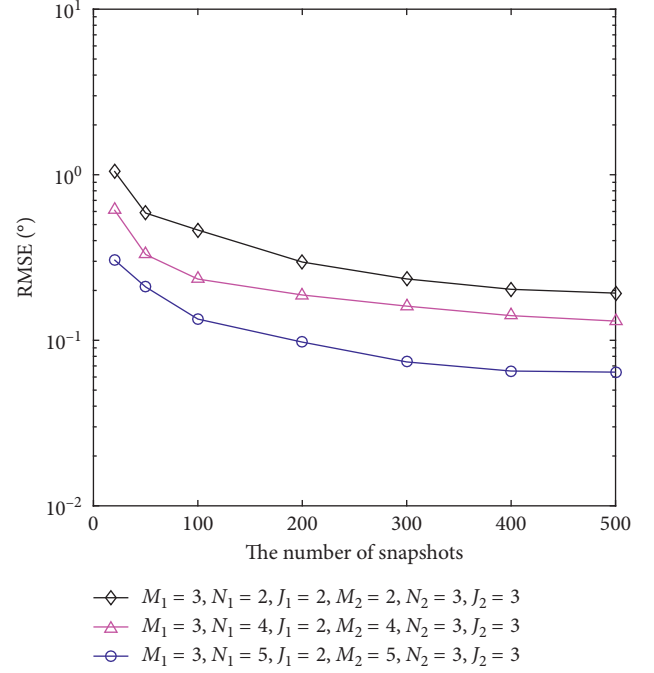


FIGURE 12: RMSE performance of different number of sensors versus snapshots.

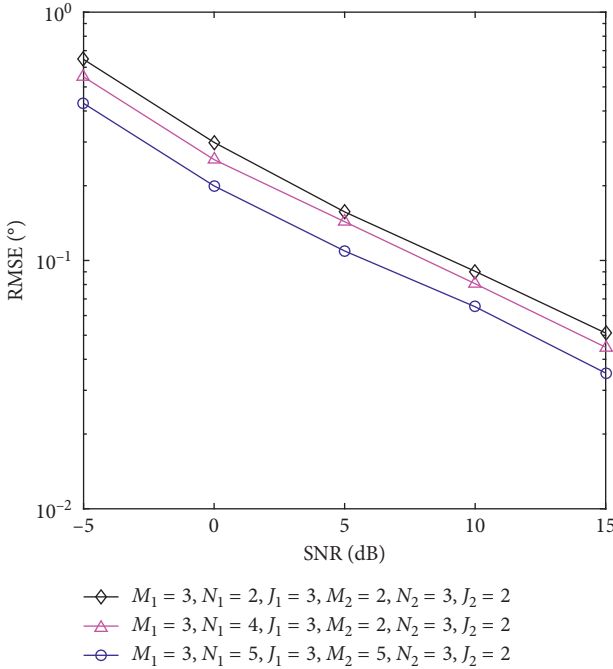


FIGURE 11: RMSE performance of different number of sensors versus SNR.

obviously shown that the RMSE estimation performance of the proposed AMRD-MUSIC algorithm is improving with the increase of SNR or snapshots due to the diversity gain.

## 6. Conclusions

In this paper, a CCA geometry in massive MIMO systems is constructed, which consists of two uniform cubic subarrays and obtains the extension of interelement spacing by selecting three pairs of coprime integers. Meanwhile, CRB for CCA is derived and the proposed CCA geometry is verified to outperform the conventional UCA geometry in 2D DOA estimation performance in massive MIMO systems. In addition, we propose a computationally efficient 2D DOA estimation algorithm via array mapping and reduced dimension for CCA. In the proposed algorithm, we utilize the array mapping and map the nonuniform array into two uniform arrays and operate the reduced dimension process on the two uniform arrays to transform the 2D SPS problem into 1D one. In addition, the computational complexity gets further reduced by converting the 1D SPS problem into a polynomial root finding problem. Numerical simulation results verify the effectiveness of the proposed algorithm that can reduce the computational complexity cost with no degradation of DOA estimation performance.

## Data Availability

No data were used to support this study.

## Conflicts of Interest

The authors declare that they have no conflicts of interest.

## Acknowledgments

This work was supported by the China NSF Grants (61971217, 61371169, 61601167), Shandong Province NSF Grants (ZR2016FM43), Key Laboratory of Dynamic Cognitive System of Electromagnetic Spectrum Space (Nanjing University of Aeronautics and Astronautics), and Ministry of Industry and Information Technology (KF20181915).

## References

- [1] H. Q. Ngo, E. G. Larsson, and T. L. Marzetta, "Energy and spectral efficiency of very large multiuser MIMO systems," *IEEE Transactions on Communications*, vol. 61, no. 4, pp. 1436–1449, 2013.
- [2] Y. Huang, S. He, S. Jin, and W. Chen, "Decentralized energy-efficient coordinated beamforming for multicell systems," *IEEE Transactions on Vehicular Technology*, vol. 63, no. 9, pp. 4302–4314, 2014.
- [3] X. Gao, L. Dai, S. Han, C.-L. I, and R. W. Heath, "Energy-efficient hybrid analog and digital precoding for mmwave MIMO systems with large antenna arrays," *IEEE Journal on Selected Areas in Communications*, vol. 34, no. 4, pp. 998–1009, 2016.
- [4] J. Zuo, J. Zhang, C. Yuen, W. Jiang, and W. Luo, "Energy-efficient downlink transmission for multicell massive DAS with pilot contamination," *IEEE Transactions on Vehicular Technology*, vol. 66, no. 2, pp. 1209–1221, 2017.
- [5] E. G. Larsson, O. Edfors, F. Tufvesson, and T. L. Marzetta, "Massive MIMO for next generation wireless systems," *IEEE Communications Magazine*, vol. 52, no. 2, pp. 186–195, 2014.
- [6] Y. Z. Su, X. W. Liu, D. Y. Li, X. B. Wang, and Y. H. Zhang, "Research on impact localization in composite materials using array signal processing and lamb wave," *Advanced Materials Research*, vol. 304, pp. 65–72, 2011.
- [7] X. Zhang, L. Xu, L. Xu, and D. Xu, "Direction of departure (DOD) and direction of arrival (DOA) estimation in MIMO radar with reduced-dimension MUSIC," *IEEE Communications Letters*, vol. 14, no. 12, pp. 1161–1163, 2010.
- [8] J. Wang, J. Chen, and D. Cabric, "Cramer-rao bounds for joint RSS/DoA-Based primary-user localization in cognitive radio networks," *IEEE Transactions on Wireless Communications*, vol. 12, no. 3, pp. 1363–1375, 2013.
- [9] X. Wang, W. Wang, X. Li, and J. Liu, "Real-valued covariance vector sparsity-inducing DOA estimation for monostatic MIMO radar," *Sensors*, vol. 15, no. 11, pp. 28271–28286, 2015.
- [10] S. Marcos, A. Marsal, and M. Benidir, "The propagator method for source bearing estimation," *Signal Processing*, vol. 42, no. 2, pp. 121–138, 1995.
- [11] J. Capon, "High-resolution frequency-wavenumber spectrum analysis," *Proceedings of the IEEE*, vol. 57, no. 8, pp. 1408–1418, 1969.
- [12] R. Schmidt, "Multiple emitter location and signal parameter estimation," *IEEE Transactions on Antennas and Propagation*, vol. 34, no. 3, pp. 276–280, 1986.
- [13] R. Roy and T. Kailath, "ESPRIT-estimation of signal parameters via rotational invariance techniques," *IEEE Transactions on Acoustics Speech and Signal Processing*, vol. 37, no. 7, pp. 984–995, 2002.
- [14] M. Pesavento, A. B. Gershman, and M. Haardt, "Unitary root-MUSIC with a real-valued eigen-decomposition: a theoretical and experimental performance study," *IEEE Transactions on Signal Processing*, vol. 48, no. 5, pp. 1306–1314, 2000.
- [15] X. Zhang, H. Wu, J. Li, and D. Xu, "Computationally efficient DOD and DOA estimation for bistatic MIMO radar with propagator method," *International Journal of Electronics*, vol. 99, no. 9, pp. 1207–1221, 2012.
- [16] F. Gao and A. B. Gershman, "A generalized ESPRIT approach to direction-of-arrival estimation," *IEEE Signal Processing Letters*, vol. 12, no. 3, pp. 254–257, 2005.
- [17] H. Chen, C. Hou, Q. Wang, L. Huang, W. Yan, and L. Pu, "Improved azimuth/elevation angle estimation algorithm for three-parallel uniform linear arrays," *IEEE Antennas and Wireless Propagation Letters*, vol. 14, pp. 329–332, 2015.
- [18] C. P. Huang and M. D. Zoltowski, "Eigenstructure techniques for 2-D angle estimation with uniform circular array," *IEEE Transactions on Signal Processing*, vol. 42, no. 9, pp. 2395–2407, 1994.
- [19] X. Zhang, W. Zheng, W. Chen, and Z. Shi, "Two-dimensional DOA estimation for generalized coprime planar arrays: a fast-convergence trilinear decomposition approach," *Multidimensional Systems and Signal Processing*, vol. 30, no. 1, pp. 239–256, 2019.
- [20] P. Pal and P. P. Vaidyanathan, "Sparse sensing with coprime samplers and arrays," *IEEE Transactions on Signal Processing*, vol. 59, no. 2, pp. 573–586, 2011.
- [21] S. Qin, Y. D. Zhang, and M. G. Amin, "Generalized coprime array configurations for direction-of-arrival estimation," *IEEE Transactions on Signal Processing*, vol. 63, no. 6, pp. 1377–1390, 2015.
- [22] P. Pal and P. P. Vaidyanathan, "Coprime sampling and the music algorithm," *Digital Signal Processing Workshop and IEEE Signal Processing Education Workshop*, pp. 289–294, 2011.
- [23] Z. Ye and C. Liu, "2D DOA estimation in the presence of mutual coupling," *IEEE Transactions on Antennas and Propagation*, vol. 56, no. 10, pp. 3150–3158, 2008.
- [24] C. Zhou, Z. Shi, Y. Gu, and X. Shen, "DECOM: DOA estimation with combined MUSIC for coprime array," *IEEE International Conference on Wireless Communication and Signal Processing (WCSP)*, pp. 1–5, 2013.
- [25] W. Zheng, X. F. Zhang, P. Gong, and H. Zhai, "DOA estimation for coprime linear arrays: an ambiguity-free method involving full DOFs," *IEEE Communication Letters*, vol. 22, no. 3, pp. 562–565, 2018.
- [26] F. Sun, B. Gao, and P. Lan, "Partial spectral search based DOA estimation method for co-prime linear arrays," *Electronics Letters*, vol. 51, no. 24, pp. 2053–2055, 2015.
- [27] D. Zhang, Y. Zhang, G. Zheng, C. Feng, and J. Tang, "Improved DOA estimation algorithm for co-prime linear arrays using root-MUSIC algorithm," *Electronics Letters*, vol. 53, no. 18, pp. 1277–1279, 2017.
- [28] Q. Wu, F. Sun, P. Lan, G. Ding, and X. Zhang, "Two-dimensional direction-of-arrival estimation for co-prime planar arrays: a partial spectral search approach," *IEEE Sensors Journal*, vol. 16, no. 14, pp. 5660–5670, 2016.
- [29] Z. Wang, Z. Xiaofei, and S. Zhan, "Two-dimensional direction of arrival estimation for coprime planar arrays via a computationally efficient one-dimensional partial spectral search approach," *IET Radars and Sonar Navigation*, vol. 11, no. 10, pp. 1581–1588, 2017.
- [30] W. Zheng, X. Zhang, and H. Zhai, "Generalized coprime planar array geometry for 2-D DOA estimation," *IEEE Communications Letters*, vol. 21, no. 5, pp. 1075–1078, 2017.
- [31] L. Xu, J. Li, and P. Stoica, "Target detection and parameter estimation for MIMO radar systems," *IEEE Transactions on*

- Aerospace and Electronic Systems*, vol. 44, no. 3, pp. 927–939, 2008.
- [32] L. Wan, G. Han, J. Jiang, J. J. P. C. Rodrigues, N. Feng, and T. Zhu, “DOA estimation for coherently distributed sources considering circular and noncircular signals in massive MIMO systems,” *IEEE Systems Journal*, vol. 11, no. 1, pp. 41–49, 2017.
  - [33] D. Nion and N. D. Sidiropoulos, “Adaptive algorithms to track the PARAFAC decomposition of a third order tensor,” *IEEE Transactions on Signal Processing*, vol. 57, no. 6, pp. 2299–2310, 2009.
  - [34] Y. Doi, K. Ichige, H. Arai et al., “3-D array configuration using multiple regular tetrahedra for high-resolution 2-D DOA estimation,” *IEEE Signal Processing Conference*, pp. 1955–1959, 2014, <http://ieeexplore.ieee.org/stamp/stamp.jsp?tp=&arnumber=6952711&isnumber=6951911>.
  - [35] H. Moriya, K. Ichige, H. Arai, T. Hayashi, H. Matsuno, and M. Nakano, “Improving elevation estimation accuracy in DOA: how planar arrays can be modified into 3-D configuration,” *IEICE Transactions on Fundamentals*, vol. E95.A, no. 10, pp. 1658–1666, 2012.
  - [36] D. Bernard, *Principles of Aperture and Array System Design*, Wiley, Hoboken, NJ, USA, 1976.
  - [37] J. Liu, Y. Zhang, Y. Lu et al., “Augmented nested arrays with enhanced DOF and reduced mutual coupling,” *IEEE Transactions on Signal Processing*, vol. 65, no. 21, pp. 5549–5563, 2017.
  - [38] D. Zhang, Y. Zhang, G. Zheng, B. Deng, C. Feng, and J. Tang, “Two-dimensional direction of arrival estimation for coprime planar arrays via polynomial root finding technique,” *IEEE Access*, vol. 6, pp. 199540–219549, 2018.
  - [39] D. Tse and P. Viswanath, *Fundamentals of Wireless Communication*, Cambridge University Press, Cambridge, UK, 2005.
  - [40] P. Stoica and A. Nehorai, “MUSIC, maximum likelihood, and Cramer-Rao bound,” *IEEE Transactions on Acoustics, Speech, and Signal Processing*, vol. 37, no. 5, pp. 720–741, 1989.
  - [41] P. Stoica and A. Nehorai, “MUSIC, maximum likelihood, and Cramer-Rao bound: further results and comparisons,” *IEEE Transactions on Acoustics, Speech, and Signal Processing*, vol. 38, no. 12, pp. 2140–2150, 1990.
  - [42] P. Stoica and A. Nehorai, “Performance study of conditional and unconditional direction-of-arrival estimation,” *IEEE Transactions on Acoustics, Speech, and Signal Processing*, vol. 38, no. 10, pp. 1783–1795, 1990.

## Research Article

# Partial ML Detection for Frequency-Asynchronous Distributed Alamouti-Coded (FADAC) OFDM

Bong-seok Kim <sup>1</sup>, Dongjun Na <sup>2</sup>, and Kwonhue Choi <sup>2</sup>

<sup>1</sup>Convergence Research Center for Future Automotive Technology, DGIST, Daegu, Republic of Korea

<sup>2</sup>Department of Information and Communication Engineering, Yeungnam University, Gyeongsan, Republic of Korea

Correspondence should be addressed to Kwonhue Choi; gonew@yu.ac.kr

Received 3 July 2019; Revised 9 August 2019; Accepted 21 August 2019; Published 30 September 2019

Guest Editor: Chan H. See

Copyright © 2019 Bong-seok Kim et al. This is an open access article distributed under the Creative Commons Attribution License, which permits unrestricted use, distribution, and reproduction in any medium, provided the original work is properly cited.

To further enhance frequency-asynchronous distributed Alamouti-coded (FADAC) orthogonal frequency division multiplexing (OFDM), we propose a new scheme which combines the partial maximum likelihood detection (PMLD) to the residual intercarrier interference cancellation (RIC). In order to decrease the performance gap from intercarrier interference- (ICI-) free level after single time iteration of the RIC, the final stage of the proposed scheme performs the PMLD limited to the symbols of less-reliable decision variables. We show that with the practically acceptable candidate symbol set size, a single iteration for RIC is enough to achieve the ICI-free performance. Moreover, the proposed scheme substantially expands the allowable ranges of the three undesirable terms, i.e., the timing and frequency offsets between the transmit antennas and the multipath delay spreads.

## 1. Introduction

Recently, distributed antenna systems (DASs) have been one of the hottest topics in 5G wireless communication systems [1–3]. In DAS, one of the main challenging issues is to mitigate self-interference due to the carrier frequency offset (FO) between the distributed transmit antennas [4–8]. In the case of DAS, the synchronization is more difficult and challenging due to the distributed nature compared to the conventional synchronization between the transmitter and receiver since each distributed transmit antenna has a different local oscillator and independent Doppler spread. The FO between the distributed transmitters destroys the designed Alamouti code property and degrades the performance. This is more significant in OFDM-modulated Alamouti code because the FO in the OFDM signals generates intercarrier interference (ICI).

In order to overcome this problem, several algorithms have been proposed [4–8]. In [4–8], the so-called frequency reversal space frequency coded OFDM has been proposed. They utilize the ICI self-cancellation property by the frequency reversal structure of the Alamouti-coded symbols

with appropriate combining technique at the receiver. However, in severely frequency-selective fading channels, these algorithms get worse because of interblock ICI terms.

Meanwhile, in [9–11], typical structures of interference cancellation algorithms for the conventional Alamouti-coded OFDM with the distributed antennas have been proposed. These algorithms generate the estimated interference terms based on the channel state and FO information and initial detection symbols. In general, ICI terms are cancelled by subtracting the estimated interference terms from the received signal. As the conventional Alamouti-coded OFDM has no ICI self-cancellation property for frequency asynchronous distributed antennas, considerable number of cancellation iterations has to be performed until the performance converges because the accuracy of the initial detection symbol is low. Moreover, the improvement of the converged performance by cancellation is not so impressive. In [12], the Alamouti-coded OFDM scheme for mitigation of ICI due to FO between two relays is proposed. The term of phase drift exists during two consecutive OFDM symbols because this scheme employs the space time code in Alamouti code schemes. In order to mitigate not only the

term of phase drift but also ICI term due to FO, the ICI cancellation methods are performed in time domain and frequency domain, respectively. Despite the complicated ICI cancellation methods, this algorithm only achieves near ICI-free performance with small FO.

Meanwhile, in [13], Kim et al. have combined a typical decision-directed iterative ICI cancellation scheme to frequency-asynchronous distributed Alamouti-coded OFDM (FADAC OFDM) shown to outperform the other existing approaches [7]. This approach achieves the considerable improvement compared to the previous ICI cancellation methods due to the far accurate initial detection of FADAC OFDM compared to those in [9–11]. From the second iteration, however, the BER is stuck in the same value and would not converge to the near ICI-free performance. In [14], in order to overcome this drawback, we have proposed a further modified version based on the selective ICI cancellation. Although the adaptive cancellation improves the performance, symbol reliability check for deciding whether or not to cancel is performed by a threshold test, which has a practical problem that the performance is very sensitive to the threshold setting. In addition, to approach the near ICI-free performance, the iterative cancellations more than 3 or 4 times are required.

In this paper, we propose an enhanced scheme for FADAC OFDM to overcome the shortcomings of [9–14]. Compared to [9–14], the proposed scheme achieves better performance even with the single-time ICI cancellation. In order to decrease the performance difference from ICI-free performance after single-time iteration of ICI cancellation, the final stage of the proposed scheme performs the partial maximum likelihood detection (PMLD) limited to the symbols of low-reliability decision variables (DVs). The selection criterion of candidate symbol set for PMLD is simply based on the power of each symbol's DV normalized by the total average power of the DV. The performance results reveal that the proposed scheme quite significantly enhances the FADAC OFDM in terms of the allowable ranges of the frequency offset and the channel selectivity.

This paper is organized as follows. We first provide the system model in Section 2 and the transceiver structure of the conventional distributed antenna Alamouti-coded OFDM with FO in Section 3. In Section 4, the proposed algorithm is addressed. We show that the proposed scheme consists of the three major stages, that is, (1) the initial detection stage using FADAC OFDM, (2) residual ICI cancellation (RIC) algorithm, and (3) PMLD algorithm. Simulation results are shown in Section 5 in order to provide the performance improvement due to the proposed algorithm. Finally, conclusions are drawn in Section 6.

## 2. The System Model

This section addresses the system model. This paper considers the distributed antenna system that is composed of two transmit (TX) antennas and one receive (RX) antenna as in [4–10]. Figure 1 shows the structure of TX and RX sides of the distributed Alamouti-coded OFDM. In Figure 1(a), let the variable  $x_{b,l}$  denote the  $l$ th data symbol of the  $b$ th subblock and  $X_{b,k}^{(A)}$  and

$X_{b,k}^{(B)}$  denote the Alamouti-coded symbols at the  $k$ th subcarrier of the  $b$ th subblock of TX antennas  $A$  and  $B$ , respectively. We will discuss more about how to perform Alamouti encoding and decoding in the next section. In each TX antenna, Alamouti-coded symbols are modulated with OFDM signals with  $N$  total subcarriers by using  $N$  point inverse Fourier transform (IFFT). Then, the OFDM modulated signals are upconverted by carrier frequencies of TX antennas  $A$  and  $B$  denoted by  $f_c^{(A)}$  and  $f_c^{(B)}$ , respectively, and transmitted from each antenna.

The TX signals from two TX antennas are received at RX antenna as shown in Figure 1(b). The RX signal is downconverted by two local carrier frequencies, i.e.,  $f_c^{(A)}$  and  $f_c^{(B)}$ , and two downconverted signals denoted by  $r^{(A)}$  and  $r^{(B)}$  are obtained, respectively. The two downconverted signals  $r^{(A)}$  and  $r^{(B)}$  are input to two  $N$ -point FFTs in order to demodulate OFDM modulated symbols, and then the two demodulated symbols at the  $k$ th subcarrier of the  $b$ th subblock of TX antennas  $A$  and  $B$  denoted by  $R_{b,k}^{(A)}$  and  $R_{b,k}^{(B)}$  are obtained from two  $N$ -point FFT outputs, respectively. By performing Alamouti decoding on  $R_{b,k}^{(A)}$  and  $R_{b,k}^{(B)}$ , the estimated symbol  $\hat{x}_l$  is finally detected.

## 3. Signal Structure of Conventional Distributed Alamouti-Coded OFDM

In this section, the signal structure of conventional distributed Alamouti-coded OFDM is illustrated. Figure 2 shows the OFDM symbol structure of the conventional distributed Alamouti-coded OFDM [9–11]. In conventional distributed Alamouti-coded OFDM, Alamouti code pairs are mapped to the consecutive subcarriers just like the typical space-frequency Alamouti code structure [15], i.e.,  $X_{b,k}^{(A)}$  and  $X_{b,k}^{(B)}$  are set to

$$\begin{aligned} X_{b,k}^{(A)} &= \begin{cases} x_{b,1}, & \text{if } k = 1, \\ -x_{b,2}^*, & \text{if } k = 2, \end{cases} \\ X_{b,k}^{(B)} &= \begin{cases} x_{b,2}, & \text{if } k = 1, \\ x_{b,1}^*, & \text{if } k = 2, \end{cases} \end{aligned} \quad (1)$$

where  $x_{b,1}$  and  $x_{b,2}$  denote the two data symbols for the  $b$ th subblock and  $(\cdot)^*$  is the complex conjugate operator.

In the RX side, two FFTs are performed on the two RX signals  $r^{(A)}$  and  $r^{(B)}$  by separately synchronizing to two asynchronous TX antenna's carrier frequencies and time delays, and two FFT outputs  $R_{b,k}^{(A)}$  and  $R_{b,k}^{(B)}$  are expressed as

$$\begin{aligned} R_{b,k}^{(A)} &= H_{b,k}^{(A)} X_{b,k}^{(A)} + \sum_{\beta=1}^{N/2} \sum_{m=1}^2 Q(2(\beta - b) + m + \varepsilon - k) \\ &\quad \cdot H_{\beta,m}^{(B)} e^{-j\theta\tau} X_{\beta,m}^{(B)} + w_{b,k}^{(A)}, \end{aligned} \quad (2)$$

$$\begin{aligned} R_{b,k}^{(B)} &= H_{b,k}^{(B)} X_{b,k}^{(B)} + \sum_{\beta=1}^{N/2} \sum_{m=1}^2 Q(2(\beta - b) + m - \varepsilon - k) \\ &\quad \cdot H_{\beta,m}^{(A)} e^{j\theta\tau} X_{\beta,m}^{(A)} + w_{b,k}^{(B)}, \end{aligned} \quad (3)$$

where  $H_{b,k}^{(A)}$  and  $H_{b,k}^{(B)}$  denote the channel fading coefficients of the  $k$ th subcarrier of  $b$ th subblock from TX antennas  $A$

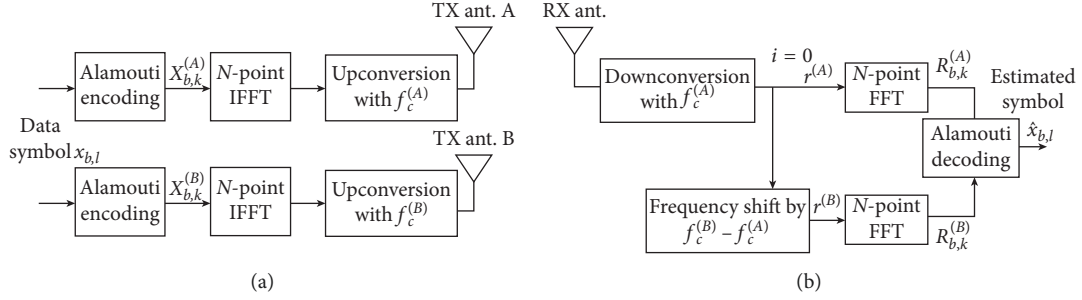


FIGURE 1: Structure of (a) TX and (b) RX sides of the distributed Alamouti-coded OFDM.

Frequency Space	(b, k)											
	(1, 1)	(1, 2)	(2, 1)	(2, 2)	(3, 1)	(3, 2)	(4, 1)	(4, 2)	...	(b, 1)	(b, n_c)	...
$X_{b,k}^{(A)}$	$x_{1,1}$	$-x_{1,2}^*$	$x_{2,1}$	$-x_{2,2}^*$	$x_{3,1}$	$-x_{3,2}^*$	$x_{4,1}$	$-x_{4,2}^*$	...	$x_{b,1}$	$-x_{b,2}^*$	...
$X_{b,k}^{(B)}$	$x_{1,2}$	$x_{1,1}^*$	$x_{2,2}$	$x_{2,1}^*$	$x_{3,2}$	$x_{3,1}^*$	$x_{4,2}$	$x_{4,1}^*$	...	$x_{b,2}$	$x_{b,1}$	...
	↑ Alamouti code symbol pair		↑ Alamouti code symbol pair		↑ Alamouti code symbol pair		↑ Alamouti code symbol pair		...	↑ Alamouti code symbol pair		

FIGURE 2: OFDM symbol structure of conventional distributed Alamouti-coded OFDM.

and  $B$ , respectively, and  $w_k^{(A)}$  and  $w_k^{(B)}$  are AWGN terms and  $Q(x)$  is the ICI coefficient. We assume that  $H_{b,k}^{(A)}$  and  $H_{b,k}^{(B)}$  are independent and follow zero mean, unit variance complex Gaussian distribution. The term  $\varepsilon$  in (2) and (3) is the normalized FO between two TX antennas, that is,  $\varepsilon = (f_c^{(B)} - f_c^{(A)})/f_\Delta$ , where  $f_\Delta$  is the subcarrier spacing. The ICI coefficient  $Q(x)$  is given as follows [16]:

$$Q(x) = \frac{\sin(\pi x)}{N \sin((\pi/N)x)} \exp\left[j\pi\left(1 - \left(\frac{1}{N}\right)x\right)\right]. \quad (4)$$

The decoding for the conventional distributed Alamouti coded OFDM is performed on  $R_{b,k}^{(A)}$  and  $R_{b,k}^{(B)}$ . The  $l$ th normalized decision variable (DV) corresponding to data symbol  $x_{b,l}$  denoted by  $\tilde{x}_{b,l}$  is obtained as follows:

$$\tilde{x}_{b,l} = \begin{cases} \frac{H_{b,l}^{*(A)} R_{b,l}^{(A)} + H_{b,l+1}^{(B)} R_{b,l+1}^{*(B)}}{|H_{b,l}^{(A)}|^2 + |H_{b,l+1}^{(B)}|^2}, & \text{for odd } l, \\ \frac{H_{b,l-1}^{*(B)} R_{b,l-1}^{(B)} - H_{b,l}^{(A)} R_{b,l}^{*(A)}}{|H_{b,l}^{(B)}|^2 + |H_{b,l+1}^{(A)}|^2}, & \text{for even } l. \end{cases} \quad (5)$$

#### 4. The Proposed Scheme

The proposed scheme in the receiver side consists of three major stages as follows:

- (1) Initial detection stage: Alamouti decoding of FADAC OFDM
- (2) RIC algorithm using the initial detection of (1)
- (3) PMLD limited to low-reliability decision variables

The following subsections explain each of these three stages, respectively.

**4.1. Initial Detection Stage: FADAC OFDM.** In FADAC OFDM, in the TX side, compared to the conventional distributed Alamouti-coded OFDM, the  $N$  total subcarriers are properly divided into the  $N_b$  subblocks according to the selectivity of the channel, and then frequency reversal Alamouti code is applied block by block, i.e., Alamouti pairs are mapped into a “mirror image” symmetric to the center frequency of each subblock as in Figure 3. Hence,  $X_{b,k}^{(A)}$  and  $X_{b,k}^{(B)}$  for  $1 \leq b \leq N_b$  are set as follows:

$$X_{b,k}^{(A)} = \begin{cases} x_{b,2k-1}, & \text{for } 1 \leq k \leq \frac{n_c}{2}, \\ -x_{b,2(n_c-k+1)}^*, & \text{for } \frac{n_c}{2} + 1 \leq k \leq n_c, \end{cases} \quad (6)$$

$$X_{b,k}^{(B)} = \begin{cases} x_{b,2k}, & \text{for } 1 \leq k \leq \frac{n_c}{2}, \\ x_{b,2(n_c-k)+1}^*, & \text{for } \frac{n_c}{2} + 1 \leq k \leq n_c. \end{cases}$$

The proposed scheme basically employs the combining scheme of the FADAC OFDM in [7] for the initial detection. In the receiver side, two FFTs are performed on  $r^{(A)}$  and  $r^{(B)}$  as in the conventional distributed Alamouti-coded OFDM and two FFT output signals as  $R_{b,k}^{(A)}$  and  $R_{b,k}^{(B)}$  are obtained. Then, the  $k$ th elements of  $b$ th subblock of them  $R_{b,k}^{(A)}$  and  $R_{b,k}^{(B)}$  are expressed as



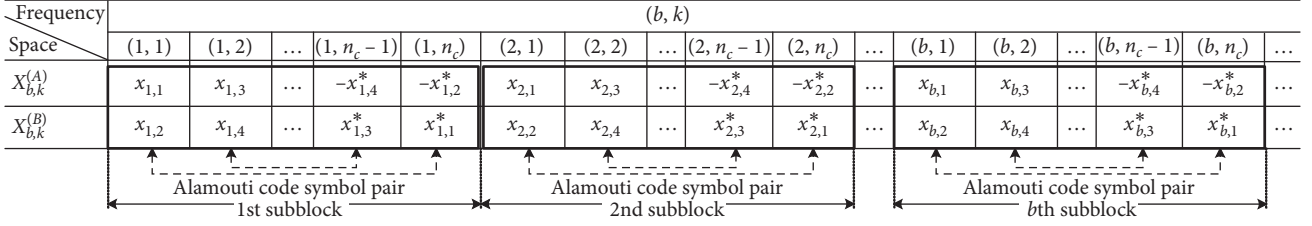


FIGURE 3: Alamouti-coded block structure of FADAC OFDM.

$$R_{b,k}^{(A)} = H_{b,k}^{(A)} X_{b,k}^{(A)} + \sum_{\beta=1}^{N_b} \sum_{m=1}^{n_c} Q((\beta - b)n_c + m + \varepsilon - k) \cdot H_{\beta,m}^{(B)} e^{-j\theta\tau} X_{\beta,m}^{(B)} + w_{b,k}^{(A)}, \quad (7)$$

$$R_{b,k}^{(B)} = H_{b,k}^{(B)} X_{b,k}^{(B)} + \sum_{\beta=1}^{N_b} \sum_{m=1}^{n_c} Q((\beta - b)n_c + m - \varepsilon - k) \cdot H_{\beta,m}^{(A)} e^{j\theta\tau} X_{\beta,m}^{(A)} + w_{b,k}^{(B)}. \quad (8)$$

We further consider the TO (timing offset) between the RX signals between the two TX antennas, which has not been considered in the previous works [13, 14]. Let  $\Delta t$  denotes the TO and we assume that OFDM symbol duration  $T$  is assumed to be sufficiently enlarged compared to  $\Delta t$  [17]. The term  $\tau$  in (7) and (8) denotes the normalized TO, i.e.,  $\tau = (\Delta t/T)$ . The terms  $e^{-j\theta\tau} X_{\beta,m}^{(B)}$  in (7) and  $e^{j\theta\tau} X_{\beta,m}^{(A)}$  in (8) denote the phase rotation of  $k$ th subcarrier of  $b$ th subblock in frequency domain due to TO  $\tau$  and  $\theta$  is calculated as  $2\pi((b-1)n_c + k - 1)$ .

The Alamouti decoding for FADAC OFDM described in [7] is performed on  $R_{b,k}^{(A)}$  and  $R_{b,k}^{(B)}$  as shown in Figure 4 and then, the normalized DVs  $\tilde{x}_{b,2k-1}$  and  $\tilde{x}_{b,2k}$  corresponding to data symbols  $x_{b,l}$  and  $x_{b,l+1}$  are obtained. By the Alamouti decoding described in [7], the normalized DVs  $\tilde{x}_{b,2k-1}$  and  $\tilde{x}_{b,2k}$  are obtained as follows:

$$\tilde{x}_{b,2k-1} = \frac{H_{b,k}^{*(A)} R_{b,k}^{(A)} + H_{b,n_c-k+1}^{(B)} R_{b,n_c-k+1}^{(B)}}{|H_{b,k}^{(A)}|^2 + |H_{b,n_c-k+1}^{(B)}|^2}, \quad (9)$$

$$\tilde{x}_{b,2k} = \frac{H_{b,k}^{*(B)} R_{b,k}^{(B)} - H_{b,n_c-k+1}^{(A)} R_{b,n_c-k+1}^{(A)}}{|H_{b,k}^{(B)}|^2 + |H_{b,n_c-k+1}^{(A)}|^2}. \quad (10)$$

For more details on the Alamouti decoding of FADAC OFDM, refer to [7].

*4.1.1. Extension of FADAC OFDM to Two RX Antennas System.* Meanwhile, in order to meet the requirement of 5G standard, we consider FADAC OFDM with two TX and two RX antennas. The overall process of this system is almost the same as in the previous system, i.e., two TX and one RX antennas, except that the number of channels and the number of FFT outputs increase as the RX signal increases. Hence, four FFT outputs are expressed as

$$\begin{aligned} R_{b,k}^{(A,A)} &= H_{b,k}^{(A,A)} X_{b,k}^{(A)} + \sum_{\beta=1}^{N_b} \sum_{m=1}^{n_c} Q((\beta - b)n_c + m + \varepsilon - k) \cdot H_{\beta,m}^{(B,A)} e^{-j\theta\tau} X_{\beta,m}^{(B)} + w_{b,k}^{(A,A)}, \\ R_{b,k}^{(B,A)} &= H_{b,k}^{(B,A)} X_{b,k}^{(B)} + \sum_{\beta=1}^{N_b} \sum_{m=1}^{n_c} Q((\beta - b)n_c + m - \varepsilon - k) \cdot H_{\beta,m}^{(A,A)} e^{j\theta\tau} X_{\beta,m}^{(A)} + w_{b,k}^{(B,A)}, \\ R_{b,k}^{(A,B)} &= H_{b,k}^{(A,B)} X_{b,k}^{(A)} + \sum_{\beta=1}^{N_b} \sum_{m=1}^{n_c} Q((\beta - b)n_c + m + \varepsilon - k) \cdot H_{\beta,m}^{(B,B)} e^{-j\theta\tau} X_{\beta,m}^{(B)} + w_{b,k}^{(A,B)}, \\ R_{b,k}^{(B,B)} &= H_{b,k}^{(B,B)} X_{b,k}^{(B)} + \sum_{\beta=1}^{N_b} \sum_{m=1}^{n_c} Q((\beta - b)n_c + m - \varepsilon - k) \cdot H_{\beta,m}^{(A,B)} e^{j\theta\tau} X_{\beta,m}^{(A)} + w_{b,k}^{(B,B)}, \end{aligned} \quad (11)$$

where  $R_{b,k}^{(U,V)}$  and  $w_{b,k}^{(U,V)}$  denote FFT output and AWGN signal of the RX signal received at the  $V$ th RX antenna ( $V \in [A \text{ and } B]$ ) and downconverted by the carrier frequency of the  $U$ th TX antenna, i.e.,  $(f_c^{(U)} \in [f_c^{(A)} \text{ and } f_c^{(B)}])$ , and  $H_{b,k}^{(U,V)}$  denotes the channel coefficient between the  $U$ th TX antenna and the  $V$ th RX antenna. The normalized DVs  $\tilde{x}_{b,2k-1}$  and  $\tilde{x}_{b,2k}$  are obtained as follows [15]:

$$\begin{aligned} \tilde{x}_{b,2k-1} &= \frac{H_{b,k}^{*(A,A)} R_{b,k}^{(A,A)} + H_{b,n_c-k+1}^{(B,A)} R_{b,n_c-k+1}^{(B,A)} + H_{b,k}^{*(A,B)} R_{b,k}^{(A,B)} + H_{b,n_c-k+1}^{(B,B)} R_{b,n_c-k+1}^{(B,B)}}{|H_{b,k}^{(A,A)}|^2 + |H_{b,n_c-k+1}^{(B,A)}|^2 + |H_{b,k}^{(A,B)}|^2 + |H_{b,n_c-k+1}^{(B,B)}|^2}, \\ \tilde{x}_{b,2k} &= \frac{H_{b,k}^{*(B,A)} R_{b,k}^{(B,A)} - H_{b,n_c-k+1}^{(A,A)} R_{b,n_c-k+1}^{(A,A)} + H_{b,k}^{*(B,B)} R_{b,k}^{(B,B)} - H_{b,n_c-k+1}^{(A,B)} R_{b,n_c-k+1}^{(A,B)}}{|H_{b,k}^{(B,A)}|^2 + |H_{b,n_c-k+1}^{(A,A)}|^2 + |H_{b,k}^{(B,B)}|^2 + |H_{b,n_c-k+1}^{(A,B)}|^2}. \end{aligned} \quad (12)$$

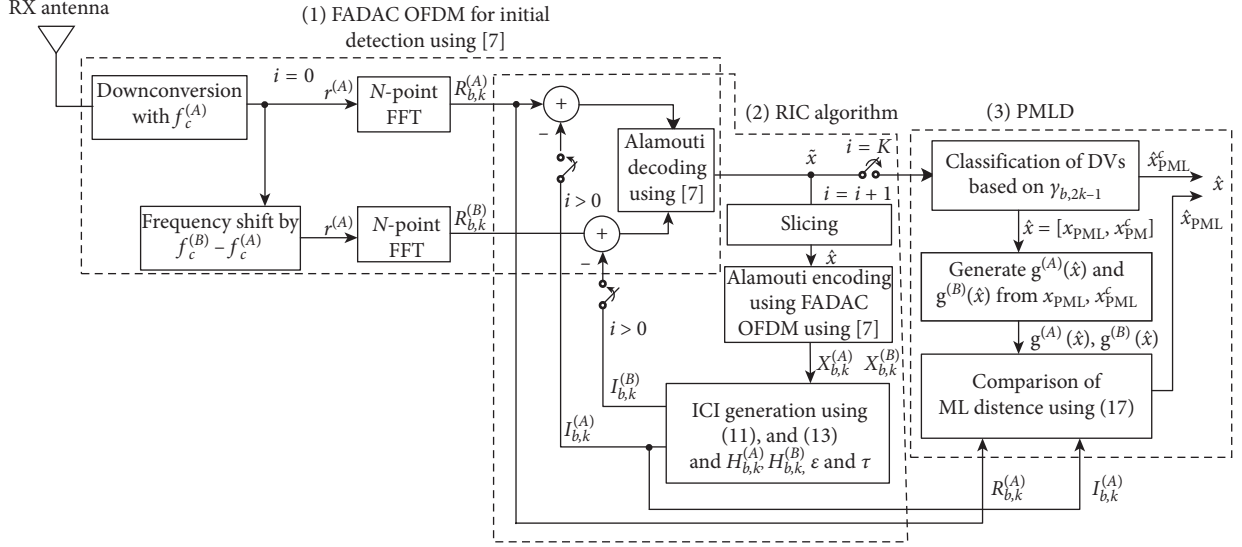


FIGURE 4: Receiver structure of the proposed scheme.

According to increase of the number of RX antennas, 3 dB gain is obtained compared with two TX antennas and one RX antenna, as is well known [15].

**4.2. RIC Algorithm.** After the initial detection, the RIC algorithm is performed. First, the estimated residual ICI terms denoted by  $I_{b,k}^{(A)}$  and  $I_{b,k}^{(B)}$  are generated in order to cancel ICI elements in the FFT output signals  $R_{b,k}^{(A)}$  and  $R_{b,k}^{(B)}$ , respectively. The estimated residual ICI terms  $I_{b,k}^{(A)}$  and  $I_{b,k}^{(B)}$  are expressed as

$$I_{b,k}^{(A)} = \sum_{\beta=1}^{N_b} \sum_{m=1}^{n_c} Q((\beta - b)n_c + m + \varepsilon - k) H_{\beta,m}^{(B)} e^{-j\theta\tau} \hat{X}_{\beta,m}^{(B)},$$

$$I_{b,k}^{(B)} = \sum_{\beta=1}^{N_b} \sum_{m=1}^{n_c} Q((\beta - b)n_c + m - \varepsilon - k) H_{\beta,m}^{(A)} e^{j\theta\tau} \hat{X}_{\beta,m}^{(A)},$$
(13)

where  $\hat{X}_{b,k}^{(A)}$  and  $\hat{X}_{b,k}^{(B)}$  are the reconstructed (estimated) versions of  $X_{b,k}^{(A)}$  and  $X_{b,k}^{(B)}$  based on the Alamouti-decoded data symbol  $\hat{x}_l$  and the transmitter structure in Figure 3. Assume that  $\varepsilon$ ,  $\tau$ , and  $\theta$  and channel coefficients  $H_{\beta,m}^{(A)}$  and  $H_{\beta,m}^{(B)}$  are known to the RX side. We update  $R_{b,k}^{(A)}$  and  $R_{b,k}^{(B)}$  by  $R_{b,k}^{(A)} - I_{b,k}^{(A)}$  and  $R_{b,k}^{(B)} - I_{b,k}^{(B)}$  which implies the residual ICI cancelled version of  $R_{b,k}^{(A)}$  and  $R_{b,k}^{(B)}$ , respectively, and then, we perform Alamouti decoding in (9) and (10) again on the updated  $R_{b,k}^{(A)}$  and  $R_{b,k}^{(B)}$ .

Unlike the previous iterative RIC schemes to FADAC OFDM in [13, 14], the proposed scheme performs the RIC just once for less computations and less demodulation latency which is a critical issue in 5G systems. In order to reduce this latency, RIC algorithm is required for just a single time. However, applying RIC algorithm for just a single time cannot achieve the performance of ICI-free level. To ameliorate this, we perform PMLD instead of the complicated successive interference cancellation algorithm in [14].

**4.3. PMLD Limited to Less-Reliable Decision Variables.** After single-time RIC stage, the final stage of the proposed scheme performs PMLD limited to the symbols of less-reliable DVs in order to enhance the performance. In order to reduce the computation load, we select only  $M (\ll N)$  least-reliable DVs as the target symbol set for PMLD. The selection criterion of candidate symbol set for PMLD is based on  $\gamma_{b,2k-1}$  and  $\gamma_{b,2k}$  which are comprised of the power of each symbols's DV normalized by the total average power of the DVs. More specifically,  $\gamma_{b,2k-1}$  and  $\gamma_{b,2k}$  for  $x_{b,2k-1}$  and  $x_{b,2k}$  are calculated, respectively as

$$\gamma_{b,2k-1} = \frac{|\text{Re}(\tilde{x}_{b,2k-1})|^2}{E[|\text{Re}(\tilde{x})|^2]},$$

$$\gamma_{b,2k} = \frac{|\text{Re}(\tilde{x}_{b,2k})|^2}{E[|\text{Re}(\tilde{x})|^2]},$$
(14)

where  $\tilde{x}$  is DV vector, i.e.,  $\tilde{x} = [x_{1,1}, x_{1,2}, \dots]$ ,  $\text{Re}(\cdot)$  denotes the real part of the complex value, and  $E(\cdot)$  denotes the expectation operator. In order to show whether  $\gamma_{b,2k-1}$  and  $\gamma_{b,2k}$  reflect the reliability of DV well, the cumulative distribution function (CDF) of  $\gamma_{b,2k-1}$  and  $\gamma_{b,2k}$  with  $N = 256$ ,  $E_b/N_0 = 10$  dB, and 20 dB with the normalized FO  $\varepsilon = 0.2$  and  $\varepsilon = 0.5$  when each DV is correctly estimated and vice versa is shown in Figure 5.

From Figure 5, the probability that the estimated symbols by RIC scheme are incorrect is about 90th percentile when  $\gamma_{b,2k-1}$  and  $\gamma_{b,2k}$  are less than 0.5. On the other hand, the probability that the estimated symbol by the RIC scheme is correct is less than 15th percentile with the same condition. This implies that almost of the estimation errors occur when  $\gamma_{b,2k-1}$  and  $\gamma_{b,2k}$  are small values. Furthermore, the probability that the estimation is incorrect is almost invariant to  $E_b/N_0$  and  $\varepsilon$ . Hence, we conclude that  $\gamma_{b,2k-1}$  and  $\gamma_{b,2k}$  are available as the simple indicator of the reliability of the DVs.

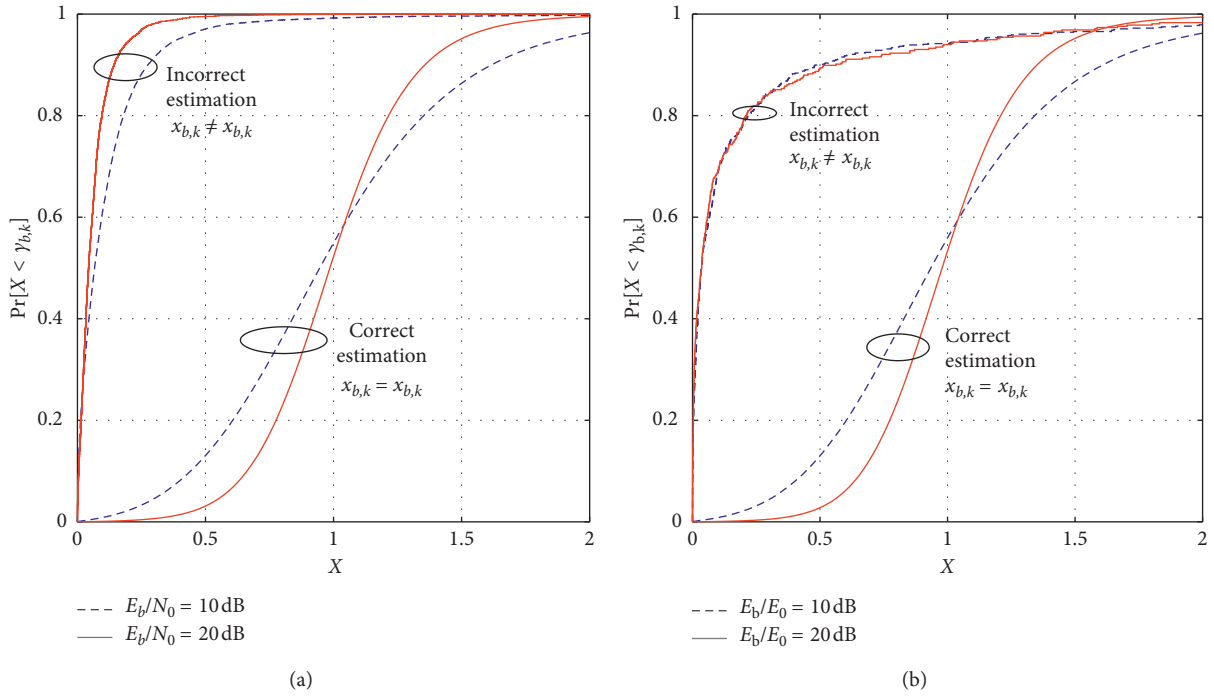


FIGURE 5: The CDF of  $\gamma_{b,2k-1}$  and  $\gamma_{b,2k}$  with QPSK and  $E_b/N_0 = 10$  dB and 20 dB.

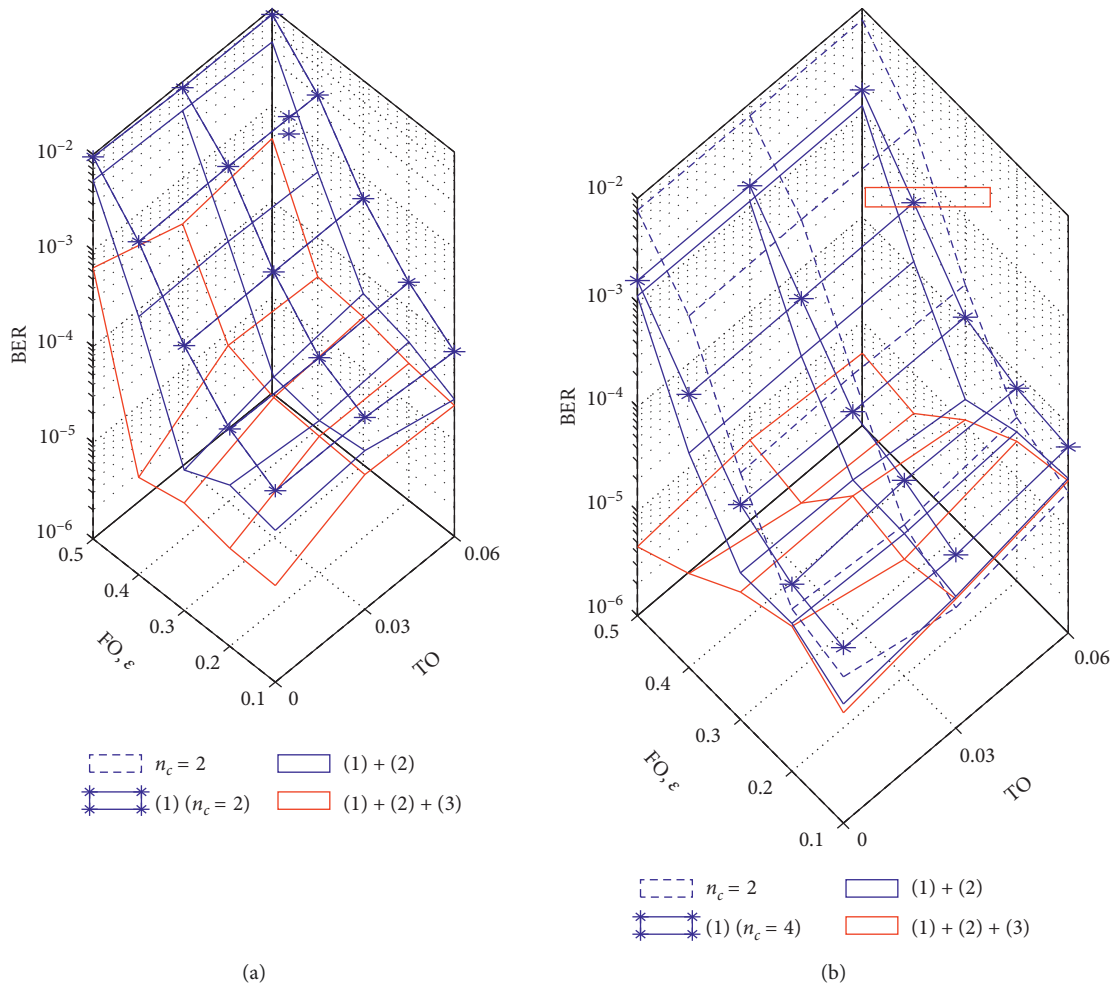


FIGURE 6: Continued.

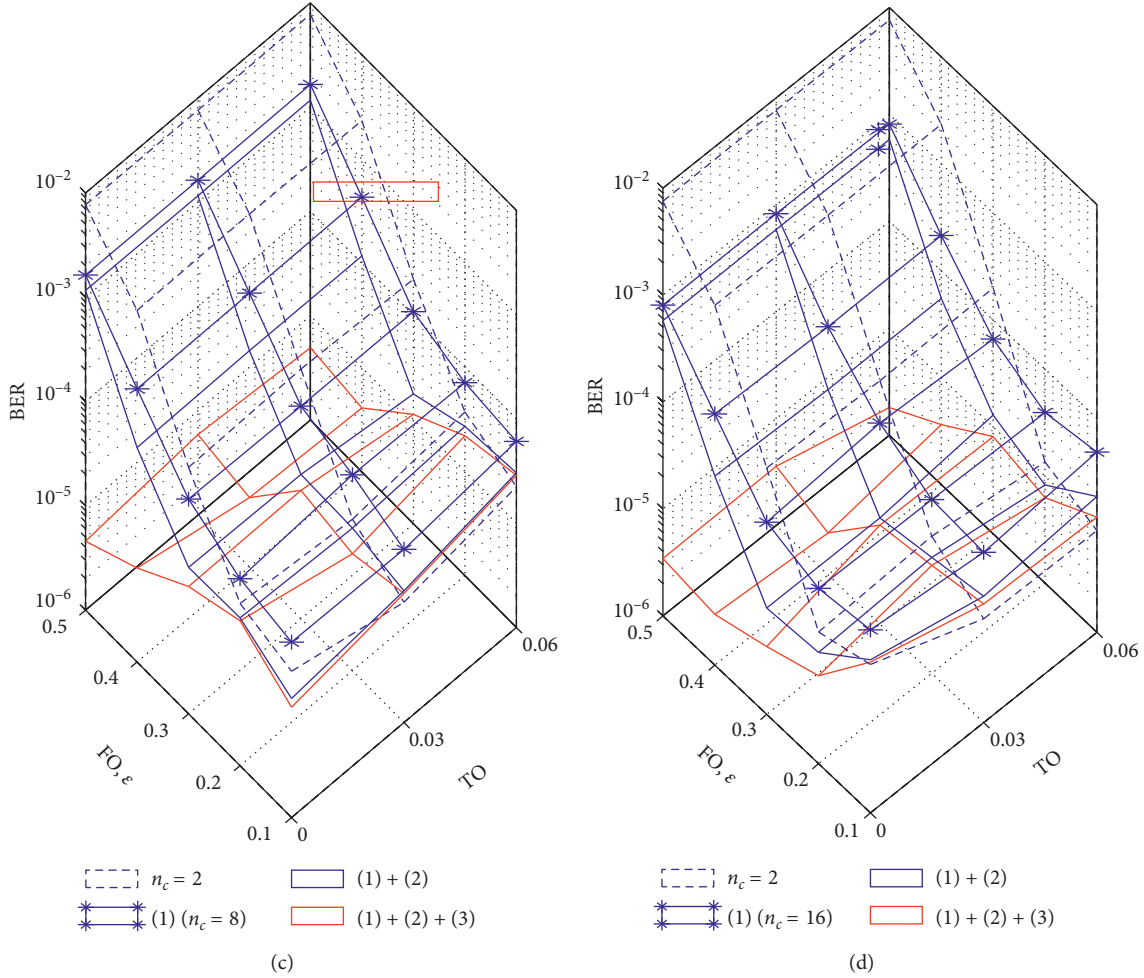


FIGURE 6: The BERs of FADAC OFDM “(1),” FADAC OFDM with SIC “(1) + (2),” the proposed scheme “(1) + (2) + (3)” with  $E_b/N_0 = 20$  dB,  $N = 256$ , and QPSK: (a)  $T_{\max} = T/10$ , (b)  $T_{\max} = T/27$ , (c)  $T_{\max} = T/50$ , and (d)  $T_{\max} = T/100$ .

Based on the observation above, the PMLD algorithm is performed using  $\gamma_{b,2k-1}$  and  $\gamma_{b,2k}$  by the following steps:

- (i) Step 1: classification of DVs for PMLD: classify the estimated DV vector  $\hat{\mathbf{x}}$  as two vectors, i.e.,  $\mathbf{x}_{\text{PML}}$  with length  $M$  and  $\mathbf{x}_{\text{PML}}^c$  with length  $N - M$  where  $\mathbf{a}^c$  is the complementary set of vector  $\mathbf{a}$ . The elements of  $\mathbf{x}_{\text{PML}}$  are classified as the symbols corresponding to the  $M$  minimum  $\gamma_{b,2k-1}$  and  $\gamma_{b,2k}$ . Meanwhile, the rest  $N - M$  symbols with high reliability, i.e.,  $\mathbf{x}_{\text{PML}}^c$ , are determined as final detection symbol in this step.

- (ii) Step 2: PMLD: in this step, the PMLD is performed only for the DVs with low reliability, i.e.,  $\mathbf{x}_{\text{PML}}$ . The detection symbol vector by PMLD  $\hat{\mathbf{x}}_{\text{PML}}$  is obtained as follows:

$$\hat{\mathbf{x}}_{\text{PML}} = \arg \min_{\mathbf{x}_{\text{PML}} \in C^M} \left\{ \left| \mathbf{r}^{(A)} - \mathbf{g}^{(A)}(\hat{\mathbf{x}}) \right|^2 + \left| \mathbf{r}^{(B)} - \mathbf{g}^{(B)}(\hat{\mathbf{x}}) \right|^2 \right\}, \quad (15)$$

where  $C$  denotes the constellation point set of the data symbol,  $\mathbf{r}^{(A)}$  and  $\mathbf{r}^{(B)}$  are FFT output vectors of  $R_{b,k}^{(A)}$  and  $R_{b,k}^{(B)}$ , i.e.,  $\mathbf{r}^{(A)} = [R_{1,1}^{(A)}, R_{1,2}^{(A)}, R_{1,3}^{(A)}, \dots,$

$R_{N_b, n_c}^{(A)}]$  and  $\mathbf{r}^{(B)} = [R_{1,1}^{(B)}, R_{1,2}^{(B)}, R_{1,3}^{(B)}, \dots, R_{N_b, n_c}^{(B)}]$ , respectively, and  $\mathbf{g}^{(A)}(\hat{\mathbf{x}})$  and  $\mathbf{g}^{(B)}(\hat{\mathbf{x}})$  are the reconstructed versions of  $\mathbf{r}^{(A)}$  and  $\mathbf{r}^{(B)}$  assuming the transmitted data vector is  $\hat{\mathbf{x}}$ . Note that the computation complexity for (15) is impractically high. Hence, we employ the following three techniques to get the reasonable complexity.

- (1) We neglect the term  $|\mathbf{r}^{(B)} - \mathbf{g}^{(B)}(\hat{\mathbf{x}})|^2$  (or the term  $|\mathbf{r}^{(A)} - \mathbf{g}^{(A)}(\hat{\mathbf{x}})|^2$ ). This is because it is intuitive that these two terms are highly redundant due to the fact that both  $\mathbf{r}^{(A)}$  and  $\mathbf{r}^{(B)}$  are obtained from the common received signal.
- (2) We perform the ML search over the  $J$  closest constellation points to the initial detection point rather than exhaustive search over all the constellation point in the set  $C$ . Hence, we scan only  $J^M$  candidate symbol vectors in the space  $C^M$  and thus the complexity reduction will be substantial for high-order modulation.
- (3) As we sequentially scan the candidate symbol vectors in the space  $C^M$  one by one, there is only one element

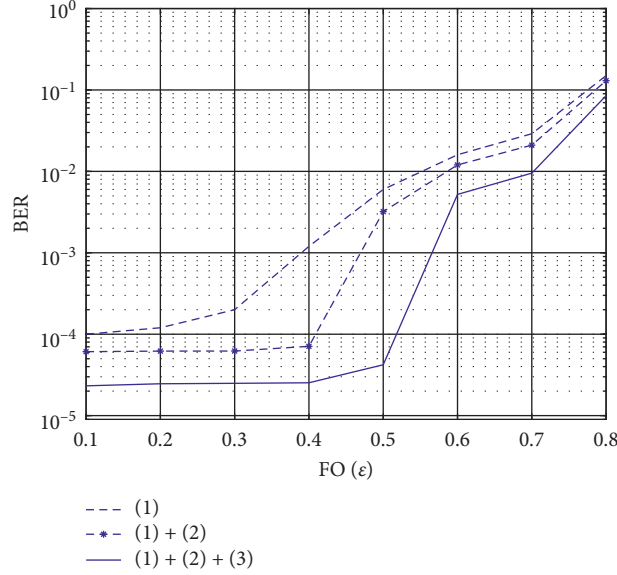


FIGURE 7: The BERs of FADAC OFDM “(1),” FADAC OFDM with SIC “(1) + (2),” the proposed scheme “(1) + (2) + (3)” with  $E_b/N_0 = 20$  dB,  $N = 256$ , QPSK, and  $T_{\max} = T/50$ .

difference between the previous candidate symbol vector and the current symbol vector. Thus, for generating  $\mathbf{g}^{(A)}(\hat{\mathbf{x}})$  (or  $\mathbf{g}^{(B)}(\hat{\mathbf{x}})$ ) in (15), we only need to generate the newly added signal component and then recursively replace the previously added component. Specifically, to update the signal parts in (7) and (8), i.e.,  $H_{b,k}^{(A)}X_{b,k}^{(A)}$  and  $H_{b,k}^{(B)}X_{b,k}^{(B)}$ , only two sign changes are required and to update the ICI terms,  $N$  subtractions and additions are required because we have already reconstructed the ICI terms in the RIC stage and we will use them as the initial values for the recursive updates. Overall, neglecting sign changes that are negligible,  $2NJ^M$  additions are required for the proposed PMLD scheme.

## 5. Simulation Results

The FADAC OFDM in [6] and its modified versions in [13, 14] has been already intensively compared to the previous distributed Alamouti-coded OFDM schemes such as the ones in [5] or [9]. Hence, in this paper, we focus on comparing the proposed scheme with the basic FADAC OFDM [6] and the FADAC OFDM with SIC in [14]. We exclude the FADAC OFDM with SIC in [13] for compactness as its upgraded version in [14] works far better. The main benefit of the proposed scheme lies in the feature that it needs RIC just once. Hence, for comparing on the same basis, the number of SIC iterations is commonly set to 1.

Figure 6 shows the BER performances of the schemes in comparison over the frequency offset and the timing offset plane for various cases of delay spread  $T_{\max}$  with  $E_b/N_0 = 20$  dB. We commonly set  $N = 256$  and use QPSK constellation. For the PMLD in the proposed scheme, we set  $J = 2$  and  $M = 4$  which needs a marginal computation overhead compared to the computations for the interference

reconstruction in the RIC stage. Regarding the multipath profile for generating  $H_{b,k}^{(A)}$  and  $H_{b,k}^{(B)}$ , the number of multipaths is 8 and their delay are distributed uniformly in  $[0 T_{\max}]$ . The guard interval is set to be larger than  $T_{\max} + \tau$ . The subcarrier spacing is set to 15 kHz which is taken from long-term evolution (LTE) standard [18]. The subblock size  $n_c$  which varies according to delay spread is taken from the results in [7].

We use the compact labels to each scheme in the legend: “(1)” for FADAC OFDM as it only uses the stage (1) in Figure 4, “(1) + (2)” for FADAC OFDM with SIC as it corresponds to the stages (1) and (2) in Figure 4, and “(1) + (2) + (3)” for the proposed scheme. For FADAC OFDM with SIC “(1) + (2),” the adaptive selection (AS) mode for interference cancellation in [14] is employed and thus, the RIC stage outperforms that of the proposed scheme although we specify it as “(1) + (2)” for easy expression. The conventional space frequency Alamouti-coded OFDM with the label  $n_c$  is also included for reference.

Note that although the FADAC OFDM with SIC “(1) + (2)” achieves the substantially improved performance compared to the basic FADAC OFDM, it still degrades significantly for larger FOs. Meanwhile, except the severely selective fading (say the case with  $T_{\max} = T/10$ ), the proposed scheme achieves near ICI-free performance for wide range of FO. This confirms that the PMLD in the final stage of the proposed scheme well fixes the errors which were not fixed in the RIC stage.

Also note that the main factor affecting the performance is FO between the two TX antennas while the BERs are almost irrespective of the timing offset (TO). Hence, for clearer view, the BER curves are plotted in two-dimension as a function of FO for two cases of fading channel selectivity. As a mildly selective fading case, we set  $T_{\max} = T/50$  in Figure 7 and as a severely selective fading case, we set  $T_{\max} = T/10$  in Figure 8. It is remarkable that the

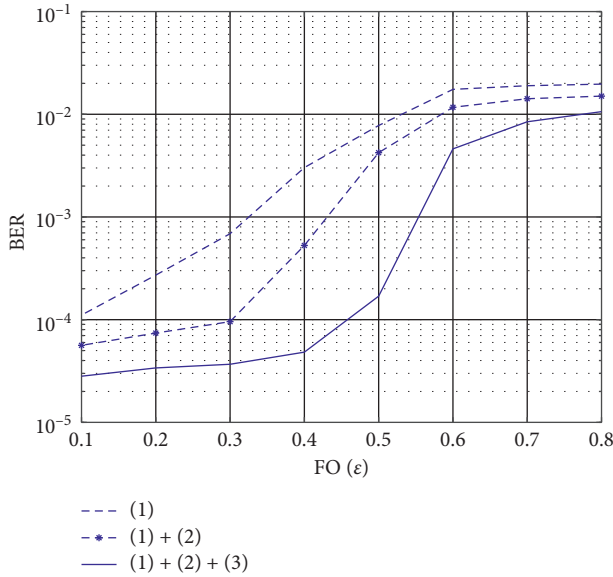


FIGURE 8: The BERs of FADAC OFDM “(1),” FADAC OFDM with SIC “(1) + (2),” the proposed scheme “(1) + (2) + (3)” with  $E_b/N_0 = 20$  dB,  $N = 256$ , QPSK, and  $T_{\max} = T/10$ .

proposed scheme significantly extends the FO range of ICI-free level even with the severe selective fading channel, i.e., up to  $FO = 0.4$  for  $T_{\max} = T/10$ . In addition, even in the small range of FO, there exist the considerable performance gaps between the proposed scheme and the other two schemes.

## 6. Conclusions

We propose a new scheme which includes RIC and PMLD in the FADAC OFDM for frequency and timing asynchronous distributed antenna systems. From simulation results, we show that additional improvement by RIC and PMLD can be dramatically accelerated with acceptable complexity. The proposed scheme achieves near ICI-free performance with wider range of FO and TO. Moreover, the proposed scheme achieves near ICI-free performance with relatively large FOs in quite selective fading channel.

## Data Availability

The matlab data used to support the findings of this study are included within the supplementary information file.

## Conflicts of Interest

The authors declare that there are no conflicts of interest regarding the publication of this paper.

## Acknowledgments

This work was supported by the DGIST R&D Program of the Ministry of Science, ICT and Future Planning, Korea (19-IT-01), the Brain Korea 21 Plus Program (No. 22A20130012814)

funded by the National Research Foundation of Korea, (NRF) and the 2018 Yeungnam University Research Grant.

## Supplementary Materials

(1) “Partial ML FADAC mfile.zip” file is source code for simulations; (2) “figures.zip” file is figure file (.eps) for latex format. (*Supplementary Materials*)

## References

- [1] C.-X. Wang, F. Haider, X. Gao et al., “Cellular architecture and key technologies for 5G wireless communication networks,” *IEEE Communications Magazine*, vol. 52, no. 2, pp. 122–130, 2014.
- [2] J. Zhang, X. Ge, Q. Li, M. Guizani, and Y. Zhang, “5G millimeter-wave antenna array: design and challenges,” *IEEE Wireless Communications*, vol. 24, no. 2, pp. 106–112, 2017.
- [3] M. Sung, J. Kim, E.-S. Kim et al., “5G trial services demonstration: IFoF-based distributed antenna system in 28 GHz millimeter-wave supporting gigabit mobile services,” *Journal of Lightwave Technology*, vol. 37, no. 14, pp. 3592–3601, 2019.
- [4] H. Wang, X.-G. Xia, and Q. Yin, “Distributed space-frequency codes for cooperative communication systems with multiple carrier frequency offsets,” *IEEE Transactions on Wireless Communications*, vol. 8, no. 2, pp. 1045–1055, 2009.
- [5] Z. Li and X. G. Xia, “An Alamouti coded OFDM transmission for cooperative systems robust to both timing errors and frequency offsets,” *IEEE Trans. Wirel. Commun.*, vol. 7, no. 5, pp. 1839–1844, 2008.
- [6] K. Choi, “Inter-carrier interference-free Alamouti-coded OFDM for cooperative systems with frequency offsets in non-selective fading environments,” *IET Communications*, vol. 5, no. 15, pp. 2125–2129, 2011.
- [7] B.-s. Kim and K. Choi, “FADAC-OFDM: frequency-asynchronous distributed alamouti-coded OFDM,” *IEEE Transactions on Vehicular Technology*, vol. 64, no. 2, pp. 466–480, 2015.
- [8] B.-s. Kim and K. Choi, “Over-sampling effect in distributed Alamouti coded OFDM with frequency offset,” *IET Communications*, vol. 10, no. 17, pp. 2344–2351, 2016.
- [9] Y. Zhang and J. Zhang, “Multiple CFOs compensation and BER analysis for cooperative communication systems,” in *Proceedings of the IEEE WCNC 2009*, Budapest, Hungary, April 2009.
- [10] T. Lu, H. Lin, and T. Sang, “An SFBC-OFDM receiver to combat multiple carrier frequency offsets in cooperative communications,” in *Proceedings of the IEEE ISPMRC 2010*, Bologna, Italy, September 2010.
- [11] J. Lee, H. Lin, and T. Sang, “An SFBC-OFDM receiver with MLSE equalizer to combat multiple carrier frequency offsets,” in *Proceedings of the IEEE ISCAS 2012*, Seoul, South Korea, May 2012.
- [12] Y. Yao and X. Dong, “Multiple CFO mitigation in amplify-and-forward cooperative OFDM transmission,” in *IEEE Transactions on Communications*, vol. 60, no. 12, 2012.
- [13] B. Kim, J. Lee, D. Jeong, and K. Choi, “Combining successive ICI cancellation to ICI suppressed Alamouti coded OFDM for frequency asynchronous distributed antenna systems,” in *Proceedings of the ITNG 2014*, Las Vegas, NV, USA, April 2014.
- [14] B. Kim and K. Choi, “Iterative detection for frequency-asynchronous distributed Alamouti-coded (FADAC)

- OFDM,” *EURASIP Journal on Wireless Communications and Networking*, vol. 2017, no. 1, 2017.
- [15] S. M. Alamouti, “A simple transmit diversity technique for wireless communications,” *IEEE Journal on Selected Areas in Communications*, vol. 16, no. 8, pp. 1451–1458, 1998.
  - [16] P. Dharmawansa, N. Rajatheva, and H. Minn, “An exact error probability analysis of OFDM systems with frequency offset,” *IEEE Transactions on Communications*, vol. 57, no. 1, pp. 26–31, 2009.
  - [17] F. Ng and X. Li, “Cooperative STBC-OFDM transmissions with imperfect synchronization in time and frequency,” in *Proceedings of the 9th Asilomar Conference on Signals, Systems and Computers*, pp. 524–528, Pacific Grove, CA, USA, October, 2005.
  - [18] S. Sesia, I. Toufik, and M. Baker, Eds., *LTE: The UMTS Long Term Evolution*, John Wiley and Sons, Hoboken, NJ, USA, 2009.